NASA TN D-1238

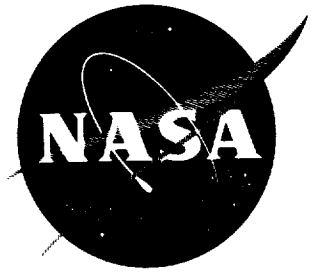

TECHNICAL NOTE

D-1238

INVESTIGATION OF VORTEX MOVEMENTS ABOUT A WING IN INTERMEDIATE AND HIGH SUBSONIC FLOW UNDERGOING A LARGE ANGLE-OF-ATTACK CHANGE IN A BLAST-INDUCED GUST

By Donald R. McFarland

Langley Research Center
Langley Station, Hampton, Va.

NATIONAL AERONAUTICS AND SPACE ADMINISTRATION
WASHINGTON
April 1962

NATIONAL AERONAUTICS AND SPACE ADMINISTRATION

TECHNICAL NOTE D-1238

INVESTIGATION OF VORTEX MOVEMENTS ABOUT A WING IN INTERMEDIATE AND HIGH SUBSONIC FLOW UNDERGOING A LARGE ANGLE-OF-ATTACK CHANGE IN A BLAST-INDUCED GUST

By Donald R. McFarland

SUMMARY

Measurements have been made of the vortex movements about an airfoil undergoing a blast of sufficient strength to exceed momentarily the stall angle by a large amount. This report extends the previously reported low-speed data to the intermediate and high subsonic velocities. A heated shock-driven tunnel was used to provide a high subsonic, steady, free jet of short duration to simulate the model flight. Small high-explosive charges were used to produce scaled blast waves.

Generally, the trailing-edge vortices travel at the fluid stream velocities, whereas leading-edge vortices travel at lower speeds. Comparison of a modified Rott theory and vortex data produced by the blast wave alone shows less agreement at the higher velocities than the low-speed data previously reported. The results indicate that the identity of the leading-edge vortex is lost in the presence of the supercritical flow over the wing model.

INTRODUCTION

With the possibility of an aircraft in flight being hit by strong blast waves from nuclear antiaircraft weapons or from a bomb delivered by the aircraft, much interest has been placed upon the blast-induced flow effect on wing loads. An investigation of the load variation on a wing of an aircraft model in low Mach number flight when subjected to a blast-induced gust from underneath was reported in reference 1. The premise that the load changes were associated with movements of the leading-edge vortex, formed at the time of blast encounter, was verified by a small-scale schlieren optical investigation of the flow. These small-scale tests made at low Mach number were reported in reference 2. (Other studies of blast-wave effects using this facility were reported in refs. 3 and 4.) Attention was recently directed to extending such studies to the higher subsonic velocities. In order to obtain the

higher velocities, the steady-flow blowdown free jet used in reference 2 was replaced with a shock-driven free-jet tunnel, since the much larger mass flow required for a steady jet was not readily available. The shock-driven tunnel provides a steady high mass flow provided by the "cold flow" (that flow originating upstream of the diaghragm) for a period of time long enough to study the transient blast-flow effects on a model immersed in the air jet of the open shock tube. Other investigations using the shock-driven tunnel technique in the study of the traveling gust effects are presented in references 5 and 6. For a general discussion of the shock-driven free-jet tunnel, see reference 7.

In the investigation presented here, flow over a rectangular airfoil set at zero lift was studied at air velocities of 400 and 800 feet per second. Flow about an airfoil was subjected to the blast from small high-explosive charges located outside the free-jet stream. The blast conditions were set up to provide a maximum resultant angle-of-attack change of 30°. A blast-alone sequence was used for comparison of the normal vortex movements. The blast-alone case provides an indication of the vortex movements without the distortions from the flow of air over the model. Similar studies have been made with shock-initiated flow by using the shock-tube tunnel. (For example, see ref. 8.)

All test conditions are summarized in table I. The orientation of the models is summarized in figure 1. All the data were obtained from schlieren pictures taken in a spanwise direction; end effects of the airfoils were neglected.

SYMBOLS

a	velocity of sound, ft/sec
b	exponent in equation (B1)
c	airfoil chord, ft
l	distance parameter in blast-wave flow, ft
M	Mach number, u/a
n	wedge-angle function, $\pi/(2\pi - \epsilon)$
p	pressure, lb/sq in.
r	distance from vortex to point of origin, ft

t	time from shock encounter with a specified point, $t = 0$ at $l = 0$ or at $r = 0$, sec
t'	time during which there has been shock-induced flow at any fixed point, sec
t_d	time duration of positive overpressure in blast, sec
T	temperature, $^{\circ}R$ or $^{\circ}F$ (when indicated)
u	fluid-flow velocity, ft/sec
u_e	equivalent-flow velocity, l/t
V	shock-wave velocity (blast front), ft/sec
x	free-stream flow displacement in chordwise direction, ft
y	free-stream flow displacement in direction normal to chord, ft
α	angle of attack of airfoil, deg
β	angle between line connecting vortex and its origin and airfoil mean line, deg
ϵ	wedge angle, deg
η	ratio of vortex displacement to free-stream fluid displacement
γ	ratio of specific heats

Subscripts:

0	initial condition before blast ($t < 0$)
2	blast flow immediately behind the wave front
3	"cold flow" region shock-tube flow
4	initial condition of pressure section of shock tube
B	blast flow
R	resultant of blast and jet flow components
X	in chordwise direction

Y	in direction normal to chord
max	maximum

APPARATUS AND TESTS

The apparatus used for these experiments was the blast-wave table of the Langley gas dynamics laboratory described in references 2 and 3. A 6-inch-diameter shock tube installed above the extended portion of the table can be seen in figure 2. A schematic diagram of the wave-table instrumentation is shown in figure 3. A blast wave was created by a 50-gram, spherically cast, bare, 50/50 pentolite charge detonated by an instantaneous electric blasting cap. The center of burst was placed 42.0 inches to 100.85 inches from the model depending upon the maximum blast-flow velocity desired for the test. The charges were centered on the blast line and at a height of 4.65 inches to insure that only a plain spherical wave could be seen in the testing area since the table-reflected wave would be combined with the initial wave. The reduced height of this charge is the same as that of the smaller pentolite charge that was used in configuration 1A and all configurations of reference 2. The pressure pickups and chronographs described in reference 3 were used to determine the blast-wave overpressure and time duration over the extended area of the table.

A 6-inch-diameter shock tube was used to set up a short duration "steady flow" over the wing model. The shock-tube axis was perpendicular to the blast line with the open end 10 inches from the blast line. Diaphragms for the shock tube were brass shim stock prescribed into quadrants. At the predetermined pressure, the diaphragm was ruptured by a hammer and plunger arrangement as can be seen at the end of the shock tube in figure 2. A 3-inch-long diaphragm section was designed to hold the ruptured diaphragm without protruding from the tube opening.

To match the density of the airjet to that of the ambient air in the room through which the blast wave had traveled, the shock-tube air was heated by means of electric resistance elements placed along the outside wall of the insulated tube. The tube air temperatures used were predetermined by the ambient air temperature and jet velocity desired. (See appendix A.) Only in the mixing zone along the jet boundaries did the air temperature not match that of ambient air. The procedure for computing the blast flow in reference 2 is repeated in appendix B. A brief discussion of the fluid displacement of the free jet under influence of the blast is given in appendix C.

The wing models were centered spanwise about the horizontal axis of the shock tube, the span being perpendicular to the wave table. The leading edge of the model was 9 inches from the open end of the shock tube and about 1 inch off the axis of the tube away from the center of burst. These distances were arrived at by taking into account the blast-wave reflection from the jet opening and lateral displacement of the jet by the blast flow. For the 10.7 pounds per square inch blast wave, the center of burst was 63 inches from the model.

The models used were rectangular planform airfoils. The first model was a symmetric 6-percent-thick wing, somewhat similar to the NACA 640006 wing section, with a chord of 0.92 inch and a span of 3.6 inches. The second model, also 6 percent thick, had a chord of 1 inch and a span of 8 inches; this model was a double-wedge airfoil having a flat lower surface and wedge leading and trailing edges over 25 percent of the chord. Both models were supported at the midchord at the one-quarter and three-quarter span locations by thin struts connected to a rigid support system. These support struts were thin in the direction of jet flow to reduce interference with the airflow and were placed upstream with respect to the blast flow to provide a clear vision of the top surface of the model and the blast-induced vortices. As the double-wedge airfoil was larger in span than the blowdown tunnel was in diameter, the ends protruded outside of the free-jet boundaries.

A single-pass schlieren optical system using 6-inch parabolic mirrors was alined parallel to the wing span and perpendicular to the surface of the wave table. A rectangular glass window, set flush with the surface of the table, permitted the light from the spark source below the table to pass over the model. The knife-edge mirror, located above the table, was shielded from the blast light as shown in figure 2. The model support and mirror mounts were attached to a vertical supporting beam independent of the wave table; thus, they were isolated from the table vibrations caused by the explosion of the charge. In sequence the charge was fired and the schlieren light source was triggered at a predetermined delay time regulating the blast-flow time over the model. Since only one photograph could be taken during a single test it was necessary to repeat tests of a given flow condition to obtain different intervals of blast-flow time over the model.

RESULTS AND DISCUSSION

Schlieren Photographs

Typical schlieren photographs of the flow about model 1 are presented in figures 4 to 7 in the same order that the test conditions are listed in table I and figure 1(a) of model orientation.

The series of photographs presented in figure 4 show the development of the edge vortices in the blast-alone flow from tests with the charge set at 90° to the airfoil. In figure 4(b) the blast front, clearly defined at $t < 144$ microseconds, lies beyond the field of view at later intervals. Expansion of the flow about both leading and trailing edges of the airfoil leads to the development of the familiar starting vortices as flow is suddenly induced over the airfoil. The vortex centers are readily identified in pictures taken at $t \leq 326$ microseconds; at $t = 700$ microseconds an area of vorticity is evident although the starting vortices under the influence of the steady decrease in flow velocity are no longer sharply defined. Other disturbances in these pictures such as the reflections of the blast wave from the model are identified on the photographs. The vortices of the stronger blast wave (fig. 4(a)) appear more massive and are displaced further in time in the high fluid velocity; conversely, the weaker blast (fig. 4(c)) produced finer vortices with less displacement with time.

In figure 5 the free-jet flow about the airfoil is shown to establish general turbulent levels in the flow from the shock tunnel and to indicate the extents of the areas of supercritical flow at the higher stream velocity.

The pictures of figure 6 were obtained when the 90° blast flow was superimposed upon the free-jet discharge from the shock tunnel. In the 400-foot-per-second-velocity flow (fig. 6(b)) the leading- and trailing-edge vortices are readily located at $t = 63$ microseconds, but at $t = 97$ microseconds only that from the trailing edge can be accurately identified and by $t = 523$ microseconds both vortices are lost. Superposition of the two flows leads to a general deterioration of the picture quality, largely as a result of increased turbulence along the jet boundaries; the blast-wave front is observed to have lost much of its sharpness in passing through and around the jet. At the higher jet velocity of 800 feet per second (fig. 6(a)) the sensitivity of the schlieren system was effectively reduced by the stronger density changes involved, thus, the vortices are rendered in greater contrast. At $t = 60$ microseconds the trailing-edge area is clear; its center, however, lies not at the center of the light area but along the bottom edge as the horizontal knife edge of the schlieren system cuts off light

from the lower half of the vortex. The leading-edge vortex is identified only as a general area. Again at $t = 535$ microseconds neither vortex can be identified.

The final series of photographs (fig. 7) shows the flow patterns developed from tests with the blast center located 30° to the airfoil chord; thus, the peak angle-of-attack change of the combined blast and free-jet flows is duplicated. This technique for simulating flight conditions has deficiencies (to be discussed later) but provides an excellent method of defining trends in vortex movement since, in the absence of other disturbances, the vortices are sharply defined and remarkably repeatable.

In general, the flow behavior over the sharp-leading-edge airfoil parallels that recorded with the round-edge model of configuration 1. Figure 8 presents example photographs of the flow about the configuration 2 airfoil for comparison with the photographs of the previous configurations. Since the span of the sharp-edge airfoil is more than twice that of configuration 1, the blast-alone vortices appear stronger in figures 8(a) and 8(e) than the corresponding counterparts in figures 4(b) and 7(b). The superimposing of the 90° blast on the free-jet flow over the sharp-edge model as seen in figures 8(c) and 8(d) is even more complicated by the extension of the model through the jet boundaries. The center of the vortex chosen for use with the data presented is that of the greatest displacement, which is presumed to be that part of the vortex in the center of the free jet.

Analysis of Data

As indicated previously, an abrupt increase in angle of attack can be obtained by initiating a blast flow normal to the free stream or, in the absence of a free stream, by setting the blast along a line inclined to the model chord at the desired angle. Although either method may produce the desired initial change in angle of attack, the resultant time histories of flow angle and velocity immediately following the blast are very different. This fact is illustrated in figure 9. In the presence of a free stream, a relatively small induced velocity results in the desired flow angle; as the velocity of the induced flow decreases with time, the angle of attack decreases. In the blast-alone flow, however, the angle of attack is independent of the blast-flow velocity. The magnitude of the resultant velocity is higher over the time of interest and the velocity change is less, for the simulated flight case, than for the 30° blast-alone case. The vortex movements are presented in terms of the local stream movements plotting the vortex position along coordinates alined to the model chord. For a brief discussion of the free-stream fluid particle displacement due to the simulated forward flow and the blast-induced flow, see appendix C.

The leading-edge vortex displacement in the chordwise direction is plotted in figure 10(a) for stream velocities of 800 and 400 feet per second. Because of the supercritical flow over the model at the higher velocity, vortex centers are not clearly defined and considerable scatter of the data is observed; horizontal lines through the data points indicate areas of uncertainty in locating the vortex. The blast-alone case on the other hand produced clearly definable vortices and resulted in little scatter of the data at either blast strength. (See fig. 10(b).) Although the blast-alone case provides only general simulation of the vortex motion about a moving airfoil encountering an external blast wave, the stability of the vortices and the ease of location aid in establishing trends in movement. In both cases the vortex is observed to move downstream at a velocity much less than the streamwise component of the resultant flow; in both cases also the vortex produced by the sharp-leading-edge model of configuration 2 moves at a much slower rate in the vicinity of the model than that of the round leading edge, configuration 1. Lateral movement in the presence of the external flow was much greater than that for the blast-alone case although in neither case did the vortex movement approach the lateral displacement of the flow. The leading-edge vortex movement normal to the chord is shown in figures 10(c) and 10(d); the maximum normal velocity components are 462 and 231 feet per second.

L 6 8 6

The trailing-edge vortex movements are presented in figure 11. Since the trailing edge is not affected by the supercritical flow region about the airfoil, the vortex formed here is easily discernible and readily followed even in the high velocity flows. The data trends in the blast-alone and blast-with-free-stream tests are generally similar, although scatter of data in the presence of the free stream precluded more than a qualitative evaluation. It will be noticed that the trailing-edge vortex moves in a chordwise direction at a speed approaching the free-stream displacement ($\eta_x \rightarrow 1$) whereas the leading-edge vortex for the same condition moves downstream at a much slower rate ($\eta_x < 1$). The trailing-edge vortex is for the most part surrounded by free-stream conditions; it is, therefore, not surprising that it should travel at free-stream displacement. The leading-edge vortex, on the other hand, is shielded on one side by the model and exposed to the free stream on the other; thus, an average expected vortex movement of one-half free-stream displacement is indicated. Another effect influencing the vortex propagation is the induced lift on the vortices by the local stream velocity about the vortices rotating in opposite directions.

The normal components of the trailing-edge vortex movements are shown in figures 11(c) and 11(d). Here again the clarity of the 30° blast-alone data provides a more definite trend in comparing the trailing-edge data to the leading edge. All the normal component data

for the trailing edge show the vortex traveling closer to the undisturbed flow movement than the leading-edge vortex.

Figure 12 is a comparison of the vortex displacement data at the various blast overpressures used for the 90° blast without the simulated forward velocity. Both leading- and trailing-edge vortices are shown. Vortex displacement seems to be about one-half of the free-stream fluid displacement. During the earlier part of the blast flow, the vortex displacement appears to be less, in relation to the free-stream displacement, for the stronger overpressure blast waves than for the weaker blast waves.

L
6
8
6

A comparison of the blast-alone data at an angle of attack of 30° for all blast-wave strengths used is shown in figure 13. The leading-edge vortex shows evidence of being trapped in the flow separation over the wing model, whereas the trailing-edge vortex is passed undisturbed into the blast flow and moves rapidly away from the airfoil. Retention of the leading-edge vortex by the airfoil is a result of low vortex-induced pressures at the airfoil surface. The stronger blast-wave vortices show more defect from free-stream fluid displacement than do the weaker blast-flow vortices.

Figures 14 to 18 were obtained by plotting the data in a non-dimensional time-distance relation. Since both chord length and the blast positive time duration were used in scaling down to the small scale of this facility, they are used to nondimensionalize the data in the distance and time relation. Both configurations 1 and 2 are shown in figure 14 for the higher velocity blast-with-flow condition. Theoretical curves for the free-stream particle displacements x_R/c and y_R/c are shown for both model configurations. The difference in the free-stream curves, of course, is due to the model chord length, 0.92 inch for configuration 1 and 1 inch for configuration 2, since the flow velocities are the same for both configurations. The intermediate velocity case for the blast-with-flow condition is shown in figure 15. Again, it can be noticed from these figures that the trailing-edge vortex travels at about the stream velocity whereas the leading-edge vortex is displaced at far less than stream particle movement.

By using again the time-distance relations, the blast alone normal to the airfoil model is shown in figure 16. Three blast-wave strengths are shown: 10.7 pounds per square inch blast overpressure in figure 16(a), 4.7 pounds per square inch blast overpressure in figure 16(b), and a lesser blast wave of 2.25 pounds per square inch overpressure by using the smaller 15-gram pentolite charge in figure 16(c). Again the free-stream particle displacement r_Y/c due to the blast wave is shown for the respective data configurations. From these plots it can be seen

that there is little distinction between leading- and trailing-edge vortex movement with time. The vortex displacement for the 30° angle-of-attack blast case, condition D, is presented as a function of time for blast overpressures of 26 pounds per square inch in figure 17 and 10.7 pounds per square inch in figure 18. These data indicate that the movement of the unrestrained trailing-edge vortex can be estimated with reasonable accuracy from consideration of the blast-flow field alone but that the leading-edge vortex, under the influence of the airfoil, moves at a much slower rate.

Figure 19 shows a comparison of the calculated vortex displacement and the actual vortex displacements for all blast overpressures used. The calculated method determined by Rott's theory (ref. 2) for predicting vortex movements in a shock tube was modified by using an equivalent velocity of the free stream in a spherical blast wave. This equivalent velocity was determined as

$$u_e(t) = \frac{l}{t} \tag{1}$$

where l is the flow length as found in figure 20 for a given blast wave and time. An equivalent wedge angle was estimated for the leading edge of each model, 24° was chosen arbitrarily for the round leading-edge model, 14° for the sharp-edge model, and 30° for the model in reference 2. Rott's equation as it was developed in reference 2 is as follows:

$$\frac{r}{a_2 t} = 2\left[\frac{nM_2 \sin n\pi \sin n\alpha \cos n\left(\beta - \frac{\epsilon}{2}\right)}{2\pi}\right]^{\frac{1}{2-n}} \tag{2}$$

The theory does not have as good agreement at the higher blast-wave strength data. However, as in figure 21, the theory does point out that a greater defect from the free-stream fluid displacement is expected as the blast strength is increased.

CONCLUDING REMARKS

Measurements have been made of the vortex movements with time of both the leading- and trailing-edge vortices formed about an airfoil at intermediate and high subsonic velocities undergoing a blast of sufficient strength to exceed momentarily the stall angle. Measurements were also obtained of a case of blast alone orientated as to produce

the same maximum resultant angle of attack and velocity as the simulated flight cases. From these measurements come the following conclusions:

The identity of the blast-induced leading-edge vortex at the high subsonic speeds is quickly lost in the supercritical flow over the models.

The leading-edge vortex in subcritical flow moves through the separated flow region near the leading edge of the model at much less than the stream velocity.

The trailing-edge vortices appear to travel at near the resultant free-stream particle velocity, and retain their identity for several chord lengths from the model.

For the stronger blast-alone case at an angle of attack of 30°, the leading-edge vortex displacement shows a greater defect relative to the resultant free-stream flow than the trailing-edge vortex. This defect increases with strength of the blast.

A comparison of the 30° blast-wave-alone data with a modified Rott theory shows less agreement at the higher and intermediate velocities than at the lower velocities previously reported.

Langley Research Center,
National Aeronautics and Space Administration,
Langley Air Force Base, Va., January 30, 1962.

APPENDIX A

COMPUTATIONS OF SHOCK-DRIVEN FREE-JET FLOW

Consider the case of a quasi-steady one-dimensional free jet caused by the breaking of a diaphragm at the end of a constant-area pressure chamber. If one assumes that the initial shock wave produced in the ambient air region near the diaphragm is rapidly dissipated because of its spherical nature, then ambient pressure can be assumed as a boundary condition for the free jet very shortly after rupture. Since an expansion wave will move into the pressure chamber, the isentropic expansion through the wave is

L
6
8
6

$$\left(\frac{p_4}{p_3}\right)^{\frac{\gamma-1}{\gamma}} = \frac{T_4}{T_3} = \left(\frac{a_4}{a_3}\right)^2 \tag{A1}$$

in terms of the original conditions in the pressure chamber. If it is further specified that the free-jet temperature must be equal to the ambient temperature, then both p_3 and T_3 in equation (A1) are ambient. By using also the classical "Riemann invariant" for the one-dimensional unsteady flow through the expansion wave, the fluid velocity may be obtained by using the following relation:

$$u_3 + \frac{2}{\gamma - 1} a_3 = u_4 + \frac{2}{\gamma - 1} a_4 \tag{A2}$$

From a solution of these relations, the initial pressure and temperature required to provide a specified velocity at the desired conditions are found, since u_4 is equal to zero and γ is considered to be 1.4 for air. Figure 22 is a plot using the foregoing relations showing jet velocities up to the sonic velocity and converting pressure and temperature from the absolute units to gage pressure and degrees Fahrenheit.

APPENDIX B

COMPUTATION OF BLAST-FLUID FLOW

Consider the case of a spherical blast wave in which it is assumed the variation of overpressure with time may be represented by the following expression up to values of $\frac{t'}{t_d} = 2$; this expression has been suggested in a number of places in the literature (for example, see ref. 9) and was found to fit closely the pressure-time curves:

$$\frac{p - p_0}{p_2 - p_0} = \frac{1 - \frac{t'}{t_d}}{e^{b\frac{t'}{t_d}}} \tag{B1}$$

where b is a constant for a given blast-wave-peak overpressure $p_2 - p_0$. Let it be assumed further that the value of b may be found by evaluating equation (B1) at $\frac{t'}{t_d} = 2$ by using values of the peak negative overpressure from reference 10. If it is assumed that, in the region behind the spherical shock wave $\left(0 < \frac{t'}{t_d} < 1.0\right)$, the fluid entropy is constant (a reasonable assumption for the weaker shock cases, $\frac{p_2}{p_0} < 2.0$), then the relation between fluid velocity and overpressure is found from Riemann's isentropic unsteady flow relations, which yields for air (when $\gamma = 1.40$):

$$\frac{u}{u_2} = 1 + \frac{5}{M_2}\left[\left(\frac{p}{p_2}\right)^{1/7} - 1\right] \tag{B2}$$

The value of M_2 is found as a function of $\frac{p_2}{p_0}$ from the Rankine-Hugoniot shock relations applied to this case.

It can be shown by numerical substitution that equations (B1) and (B2) are very closely satisfied over a range of blast-wave overpressures, $0 < p_2 - p_0 < 20$ psi, by the following relation:

$$\frac{u}{u_2} = \frac{1 - \frac{t'}{t_d}}{e^{\frac{1}{2}\frac{t'}{t_d}}} \qquad (B3)$$

This equation then represents an approximation of the variation of fluid velocity at any fixed reference point, the time being measured from the time of shock passage at this same point. In order more readily to find the position with time of a particular particle of fluid, the time is now referenced to that of shock passage at a specified fixed point and certain simplifications are made. (See sketch.)

L
6
8
6

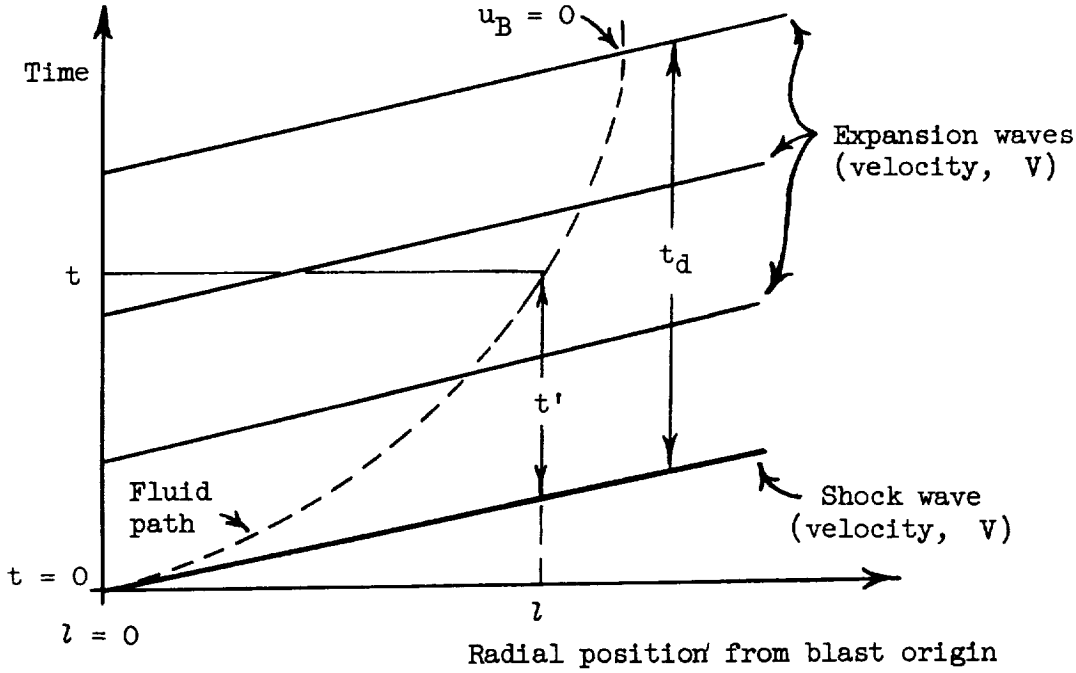

It is here assumed that over a short increment of the total blast travel, the shock travel may be assumed to be at a constant speed. Likewise, the expansion waves, following the shock, are assumed to travel at the same constant speed. Restated, the assumption is simply one of constant shock strength and positive time duration over this increment of space and should be a good assumption for the weaker shock cases and small increments of space. With this model, the following relations are written for the path of a fluid particle starting from $l = 0$ at time $t = 0$:

The fluid velocity at t is

$$u = \frac{dl}{dt} \tag{B4}$$

The fluid time to reach l is

$$t = t' + \frac{l}{V} \tag{B5}$$

The variation of fluid velocity with blast time t' at l is already given by equation (B3).

The flow distance l is given by integration of equation (B4) as

$$l = \int dl = \int_0^t u(t)dt$$

and is accomplished by first substituting for dt by differentiating equation (A5) and inserting $u(t')$ from equation (B3) and solving for dl to give equation (B4) in nondimensional form. Thus,

$$\frac{dl}{Vt_d} = \frac{1}{\frac{V}{u_2}\frac{e^{\frac{1}{2}\frac{t'}{t_d}}}{1 - \frac{t'}{t_d}} - 1} \, d\left(\frac{t'}{t_d}\right) \tag{B6}$$

Equation (B6) is integrated to give l as a function of t' and equation (B5) is then substituted into the resulting relation to give l as a function of t. The resulting fluid paths for a few blast-wave overpressures are shown in figure 20 and were obtained by integration of equation (B6), by the method of finite differences.

APPENDIX C

COMBINED FREE-JET AND BLAST-FLUID FLOWS

The theoretical displacement of the free-stream fluid particle during a given time from blast arrival was computed. In the case of the component due only to the free-jet or flight-stream fluid movement, the stream fluid displacement was obtained simply as a constant stream velocity multiplied by the time. However, for the free-stream fluid movement due to the blast a more complex computation was required because of the time-dependent nature of the flow induced by a spherically diverging wave system. This computation involved integration of an analytical approximation for the time dependency of flow velocity in the blast and was given in appendix B.

The free-stream fluid displacements in a chordwise and normal direction, respectively, are then found for all the configurations from the following general equations:

$$x_R = u_3 \cos \alpha_3 t + l \cos \alpha_B \qquad (C1)$$

$$y_R = u_3 \sin \alpha_3 t + l \sin \alpha_B \qquad (C2)$$

The value of $l = f(t)$ is found in figure 20 and computed by the method in appendix B and by using the other parameters of blast-wave-front velocity V and positive time duration t_d that are found in table I.

Specifically for the present work here with angle of attack at 0° to the jet flow and the blast at 90°, the equations become simply:

$$x_R = u_3 t \qquad (C3)$$

$$y_R = l \qquad (C4)$$

REFERENCES

1. Pierce, Harold B., and Reisert, Thomas D.: Initial Experimental Investigation of the Aerodynamic Load on the Wing of a Model Caused by a Blast-Induced Gust That Increases the Angle of Attack Into the Stall Region. NACA RM L55H22b, 1955.

2. McFarland, Donald R., and Huber, Paul W.: Investigation of Vortex Movements About a Wing in Steady Subsonic Flow Undergoing a Large Angle-of-Attack Change in a Blast-Induced Gust. NACA RM L57K04, 1958.

3. Huber, Paul W., and McFarland, Donald R.: Effect of Surface Roughness on Characteristics of Spherical Shock Waves. NASA TR R-23, 1959. (Supersedes NACA RM L55B04.)

4. McFarland, Donald R.: Investigation of Spherical-Wave-Initiated Flow Fields Around Bodies. NASA MEMO 1-6-59L, 1959.

5. Pierce, Harold B. (With Appendix by Richard W. Morton): Interaction of Blast Waves With Wings - Part I. Ten-Foot Diameter Free Jet Shock Tube. Proc. Third Shock Tube Symposium, SWR-TM-59-2, U.S. Air Force, Mar. 1959, pp. 271-291.

6. McFarland, Donald R.: Interaction of the Blast Wave With Wings - Part II. Wave-Table Studies. Proc. Third Shock Tube Symposium, SWR-TM-59-2, U.S. Air Force, Mar. 1959, pp. 293-300.

7. Ludwieg, Hubert: Der Rohrwindkanal. Z. Flugwissenchaften, Bd. 3, Heft 7, 1955, pp. 206-216.

8. Ruetenik, J. Ray: Evaluation of Traveling-Gust Method for Airfoils in Strong Blast Waves by Shock-Tube Tests. WADD Tech. Rep. 60-279, U.S. Air Force, May 1960.

9. Armendt, B. F., Smith, R., and Wise, R. C.: The Initial Decay of Pressure Behind a Shock Front: Comparison of Experimental and Calculated Results. MEMO. Rep. No. 997, Ballistic Res. Labs., Aberdeen Proving Ground, Apr. 1956.

10. Curtis, Wesley: Free Air Blast Measurements on Spherical Pentolite. MEMO. Rep. No. 544, Ballistic Res. Labs., Aberdeen Proving Ground, July 1951.

TABLE I

TEST CONDITIONS

Configuration	Condition	Model chord orientation		Blast wave				Jet flow	Resultant flow	
		With blast flow, α_B, deg	With jet flow, α_0, deg	Peak overpressure, $p_2 - p_0$, lb/sq in.	Positive time durations, t_d, microsec	Peak flow velocity, u_2, ft/sec	Wave front velocity, V, ft/sec	Flow velocity, u_3, ft/sec	Maximum α_R, deg	Flow velocity, $u_{R,max}$, ft/sec
Present test data										
1A	A1	90	---	10.7	1,010	462	1,445	---	90	462
1A	A2	90	---	4.7	1,370	231	1,280	---	90	231
1A	A3	90	---	2.25	1,085	117	1,205	---	90	117
1B	B1	---	0	-----	-----	---	-----	800	0	800
1B	B2	---	0	-----	-----	---	-----	400	0	400
1C	C1	90	0	10.7	1,010	462	1,445	800	30	924
1C	C2	90	0	4.7	1,370	231	1,280	400	30	462
1D	D1	30	---	26.0	740	924	1,800	---	30	924
1D	D2	30	---	10.7	1,010	462	1,445	---	30	462
2A	A2	90	---	4.7	1,370	231	1,280	---	90	231
2B	B1	---	0	-----	-----	---	-----	800	0	800
2C	C1	90	0	10.7	1,010	462	1,445	800	30	924
2C	C2	90	0	4.7	1,370	231	1,280	400	30	462
2D	D2	30	---	10.7	1,010	462	1,445	---	30	462
Data from reference 2										
1		86	0	1.3	1,200	69	1,180	113	30	137
2		86	0	1.3	1,200	69	1,180	113	30	137
3		86		1.3	1,200	69	1,180	0	86	69
4		31		1.3	1,200	69	1,180	0	31	69
5		31		2.65	1,040	136	1,215	0	31	136

	Condition	Angle of attack due to blast flow, α_B, deg	Peak blast flow velocity, u_2, ft/sec	Free jet flow velocity, u_3, ft/sec
Configuration 1A				
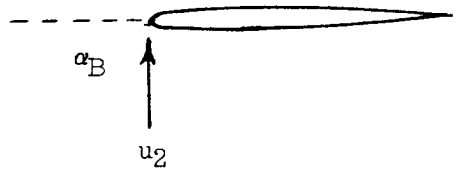	A1	90	462	-
	A2	90	231	-
	A3	90	117	-
Configuration 1B				
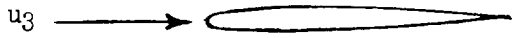	B1	-	-	800
	B2	-	-	400
Configuration 1C				
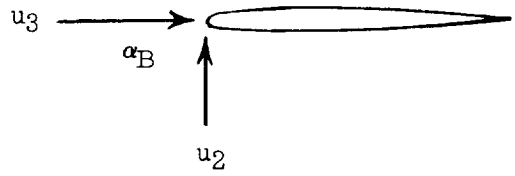	C1	90	462	800
	C2	90	231	400
Configuration 1D				
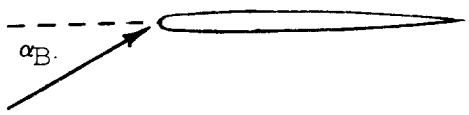	D1	30	924	-
	D2	30	462	-

(a) Configuration 1.

Figure 1.- Model orientation.

	Condition	Angle of attack due to blast flow, α_B, deg	Peak blast flow velocity, u_2, ft/sec	Free jet flow velocity, u_3, ft/sec
Configuration 2A				
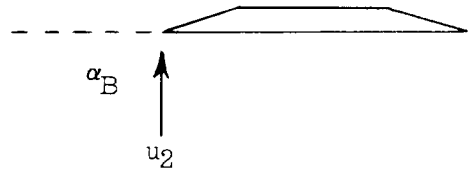	A2	90	231	-
Configuration 2B				
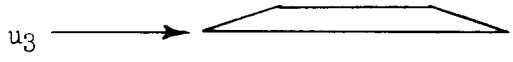	B1	-	-	800
Configuration 2C				
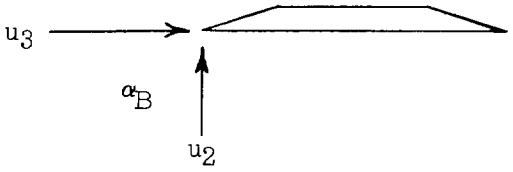	C1	90	462	800
	C2	90	231	400
Configuration 2D				
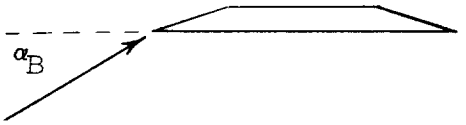	D2	30	462	-

(b) Configuration 2.

Figure 1.- Concluded.

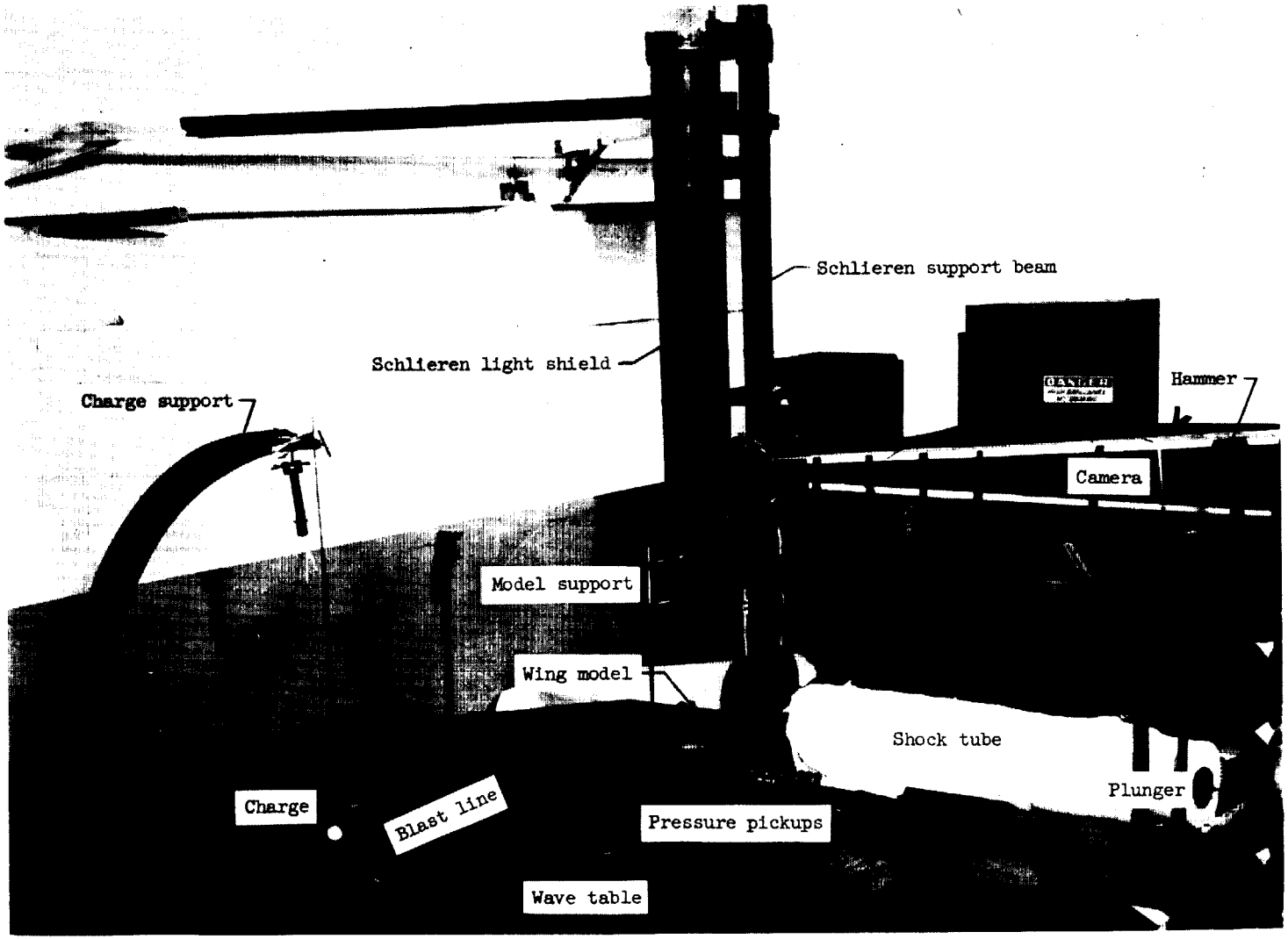

Figure 2.- Photograph of wave-table arrangement. L-59-2060.1

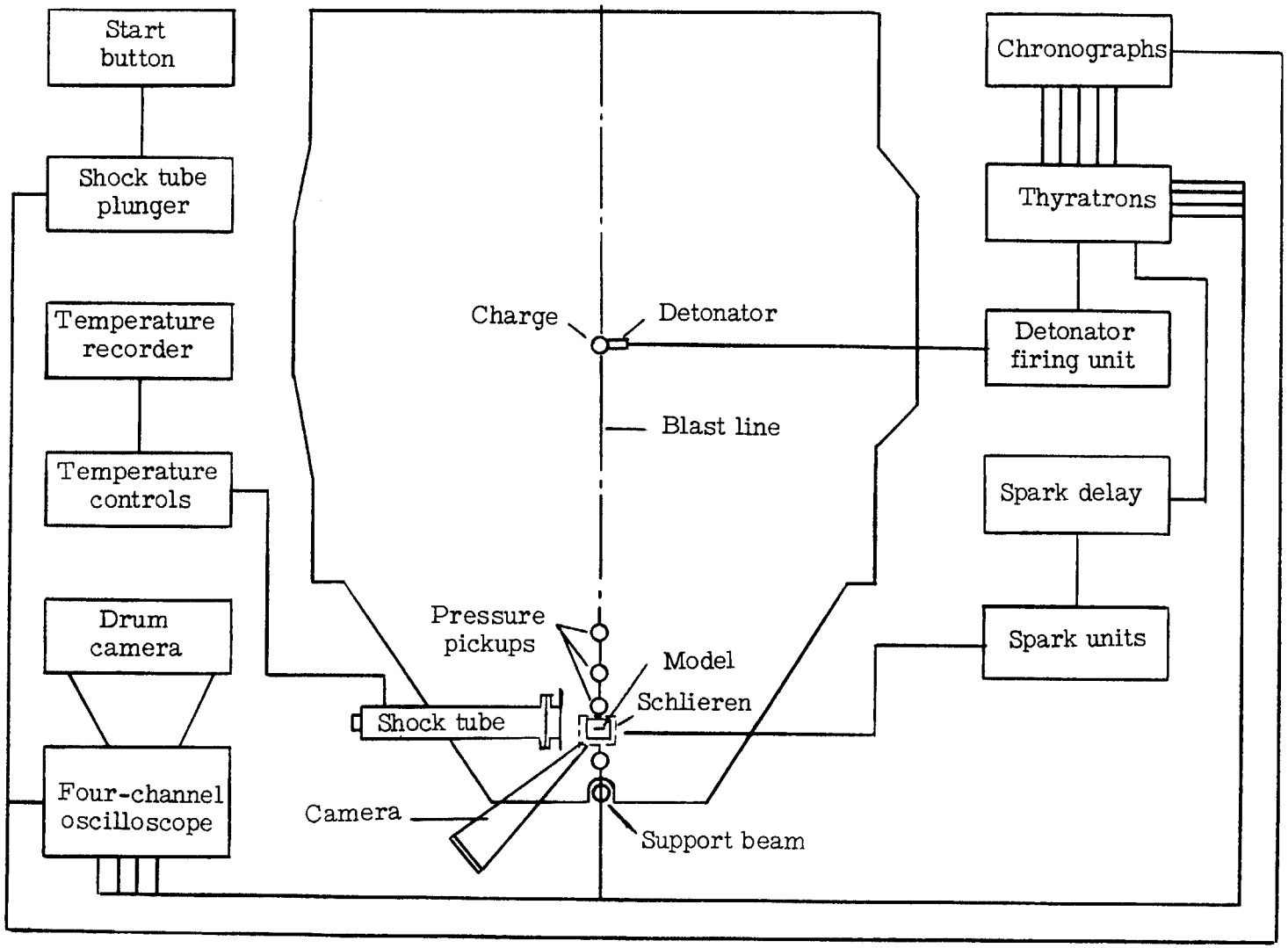

Figure 3.- Schematic of wave table and instrumentation.

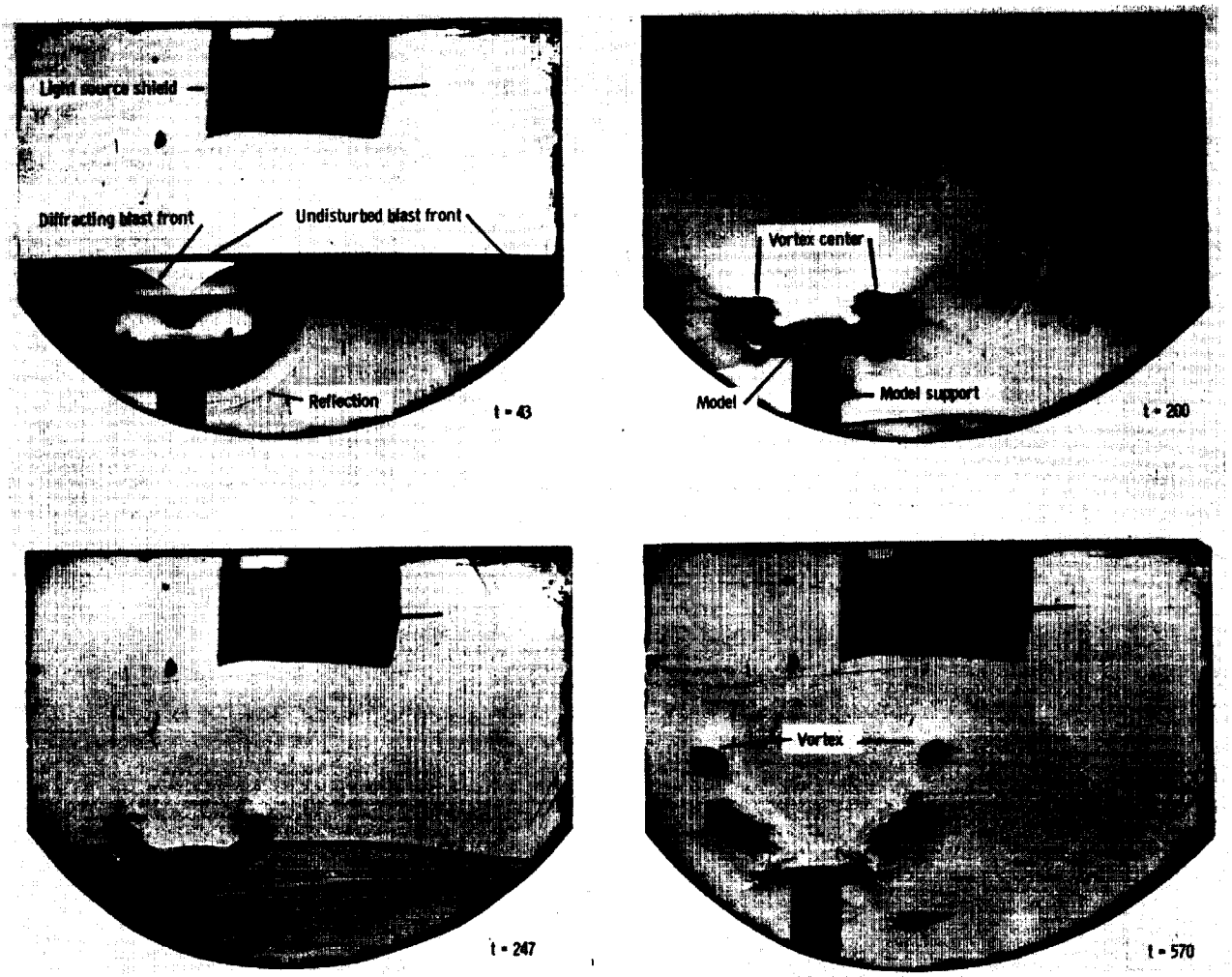

(a) A sequence of condition A1; peak blast flow, 462 feet per second. L-62-33

Figure 4.- Schlieren photographs of configuration 1A; blast flow $\alpha_B = 90^\circ$; no jet flow; time t is given in microseconds; each photograph represents a separate test.

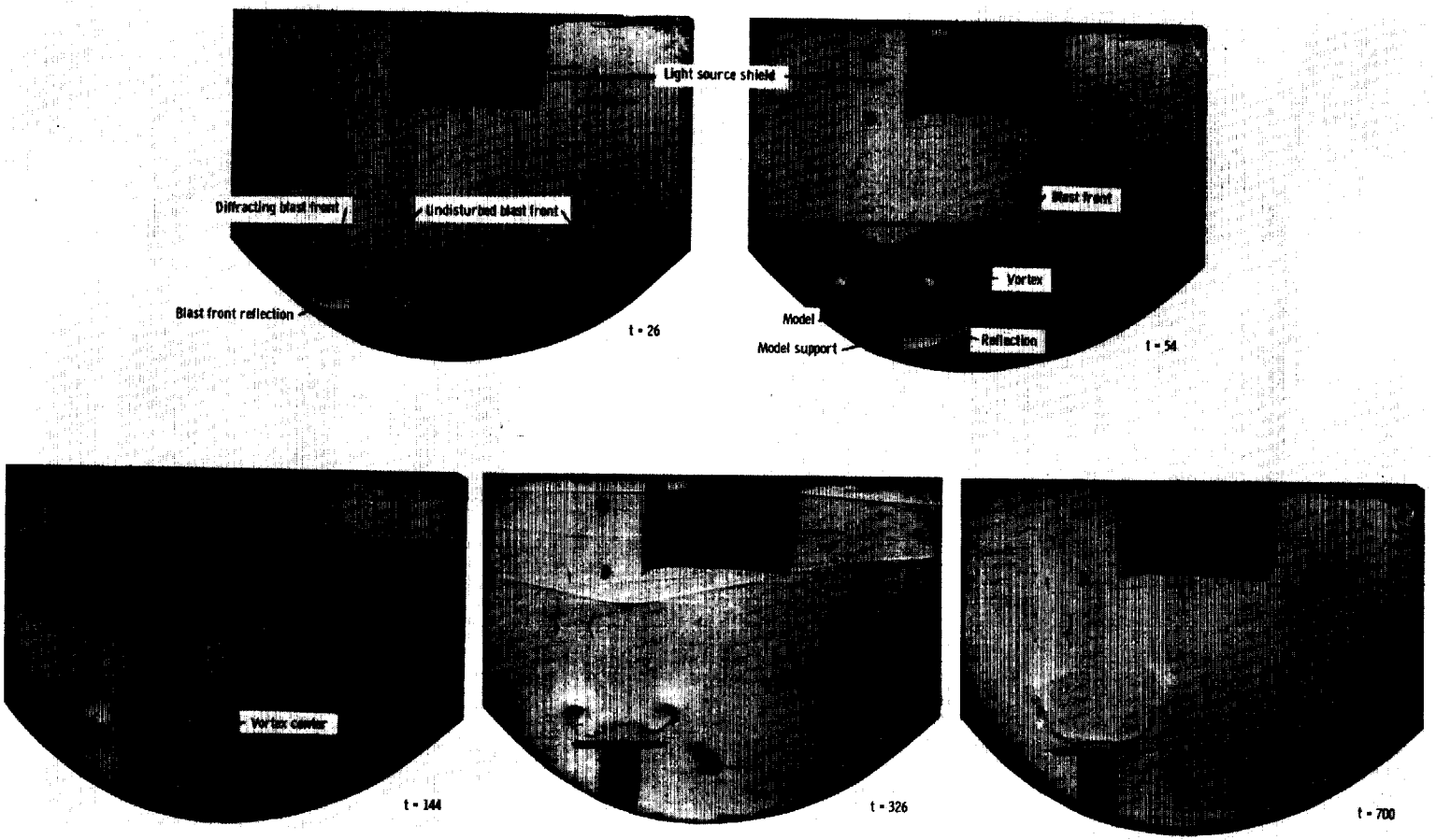

(b) A sequence of condition A2; peak blast flow, 231 feet per second. L-62-34

Figure 4.- Continued.

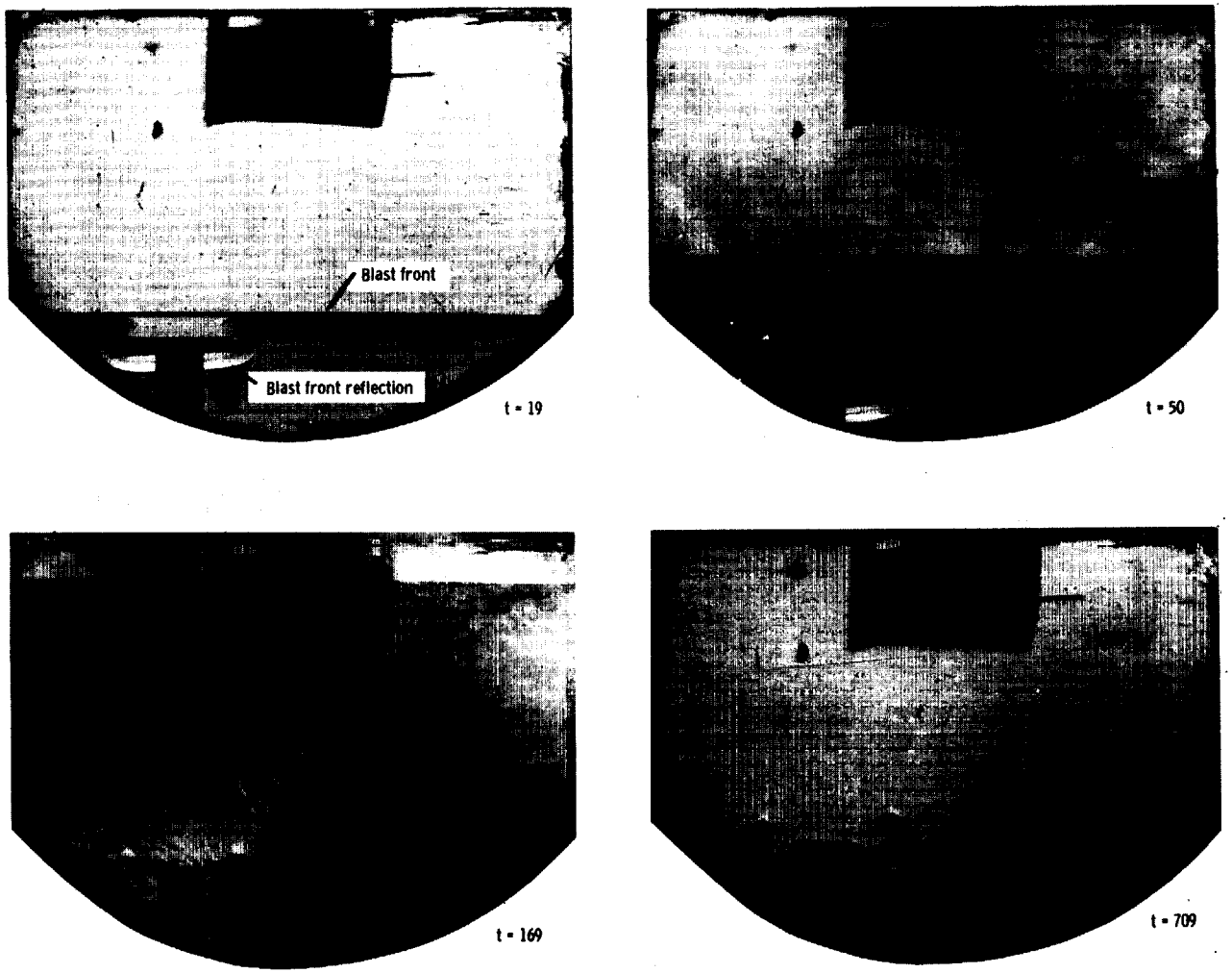

(c) A sequence of condition A3; peak blast flow, 117 feet per second. L-62-35

Figure 4.- Concluded.

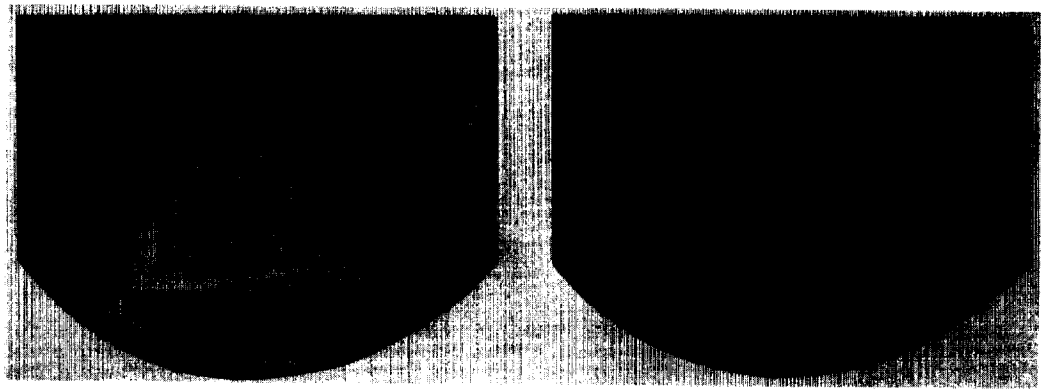

L-62-36

(a) Condition B1; jet flow, 800 feet per second.

(b) Condition B2; jet flow, 400 feet per second.

Figure 5.- Schlieren photographs of configuration 1B; jet flow, no blast flow.

L-62-37

(a) Condition C1; peak blast flow, 462 feet per second; jet flow, 800 feet per second.

Figure 6.- Schlieren photographs of configuration 1C, combined blast flow $\alpha_B = 90^\circ$ and jet flow; time t is given in microseconds; each photograph represents a separate test.

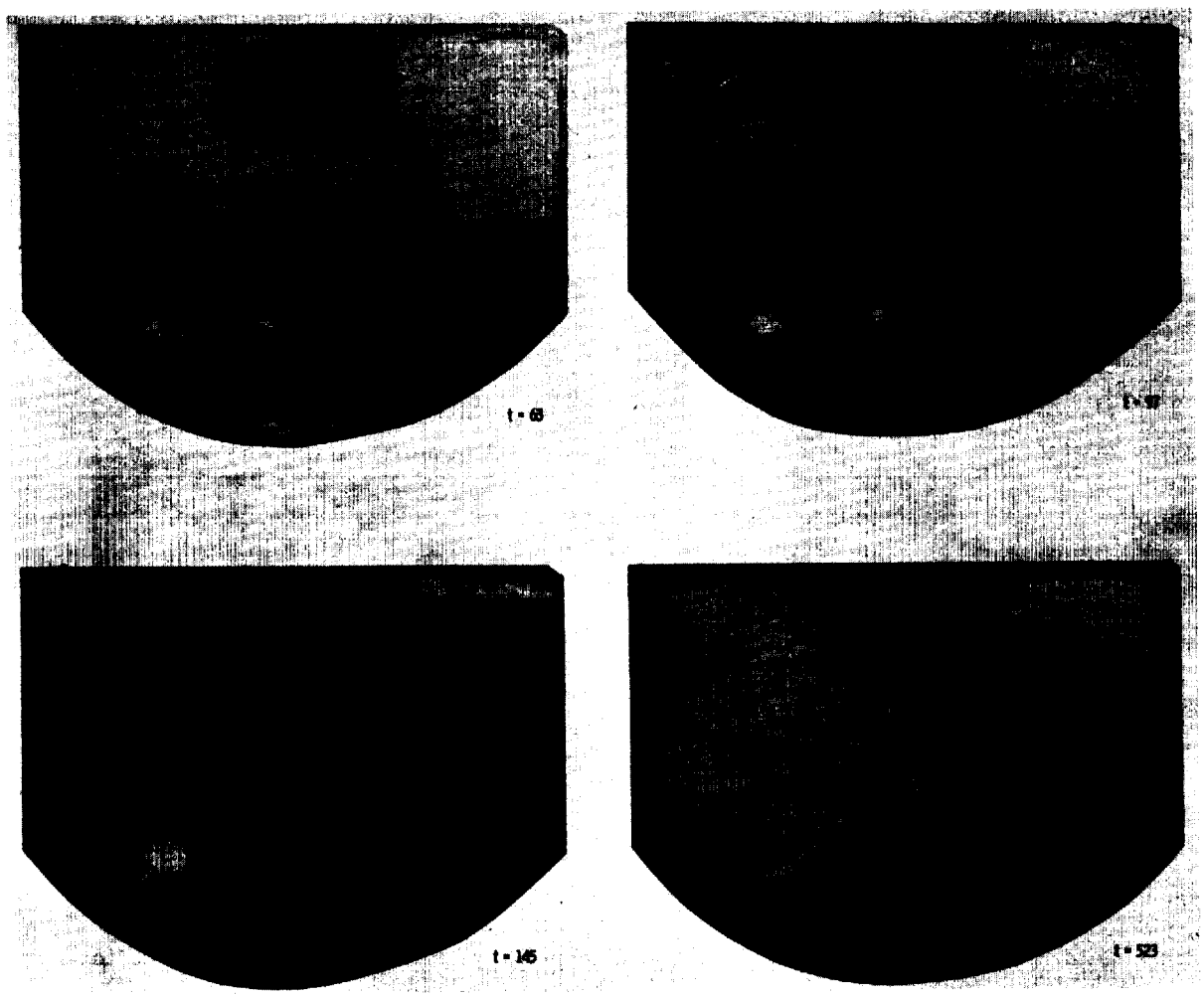

L-62-38

(b) Condition C2; peak blast flow, 231 feet per second; jet flow, 400 feet per second.

Figure 6.- Concluded.

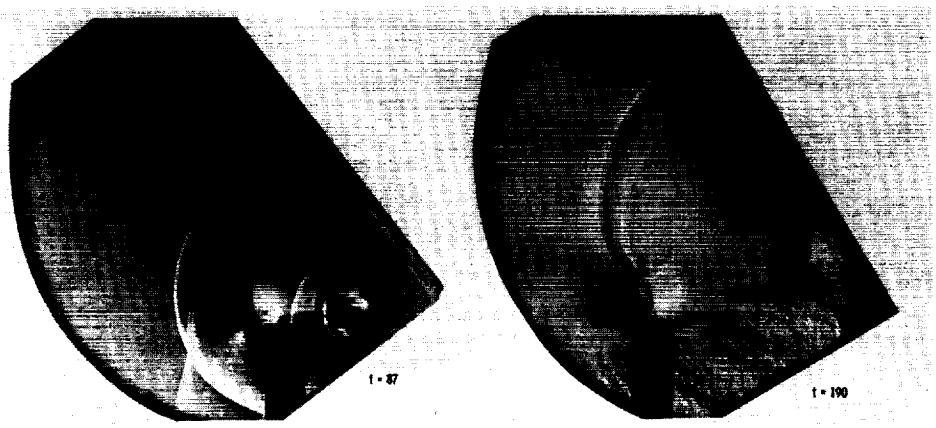

(a) Condition D1; peak blast flow, 924 feet per second.

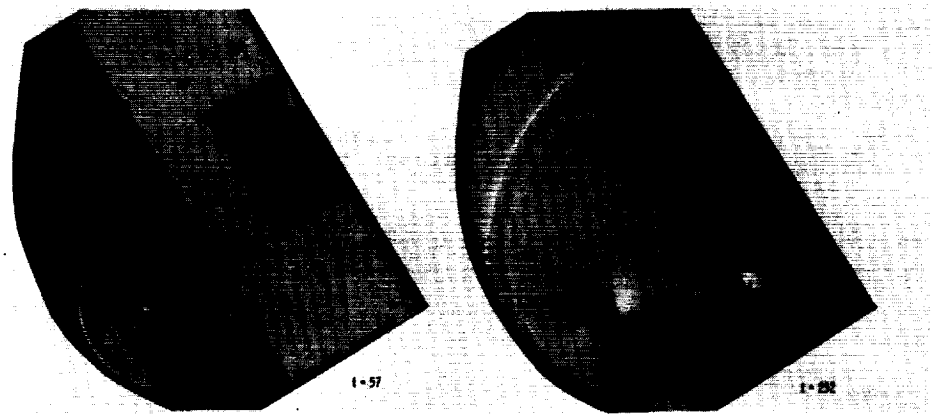

(b) Condition D2; peak blast flow, 462 feet per second.

L-62-39

Figure 7.- Schlieren photographs of configuration 1D; blast flow, $\alpha_B = 30^\circ$; no jet flow; time t is given in microseconds; each photograph represents a separate test.

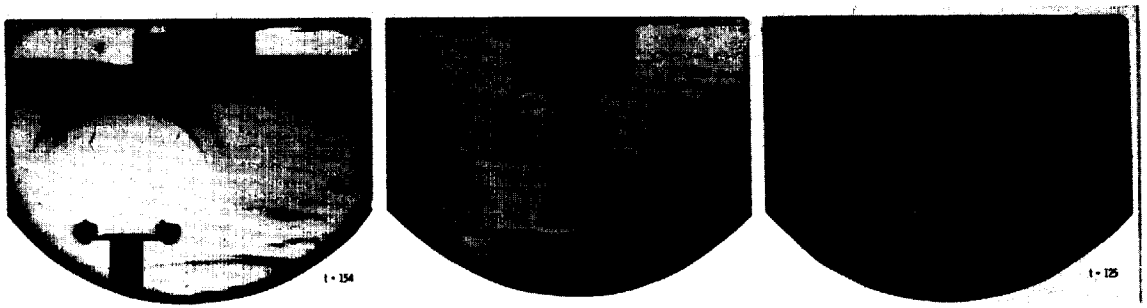

(a) Condition A2; peak blast flow, 231 feet per second; $\alpha_B = 90^\circ$.

(b) Condition B1; jet flow, 800 feet per second.

(c) Condition C1; peak blast flow, 462 feet per second; jet flow, 800 feet per second.

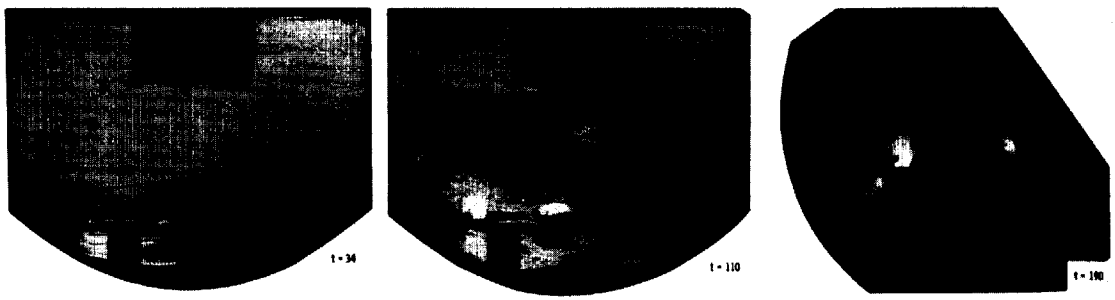

(d) Condition C2; peak blast flow, 231 feet per second; jet flow, 400 feet per second.

(d) Concluded.

(e) Condition D2; peak blast flow, 462 feet per second; $\alpha_B = 30^\circ$.

Figure 8.- Typical photographs of configuration 2. L-62-40

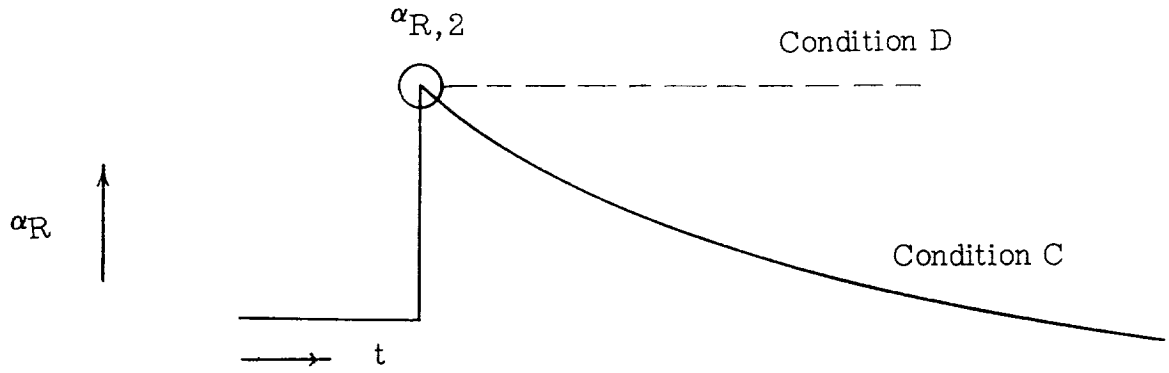

(a) Angle of attack plotted against time.

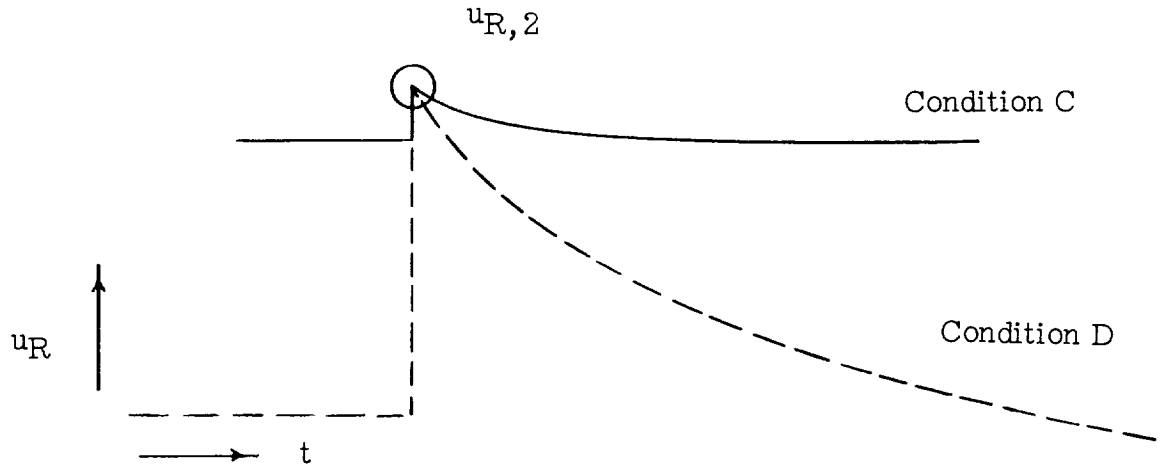

(b) Resultant velocity plotted against time.

Figure 9.- Time history of resultant angle of attack and resultant velocity for blast in flight (condition C) and blast over a stationary model, with simulation of maximum resultant velocity and angle of attack (condition D).

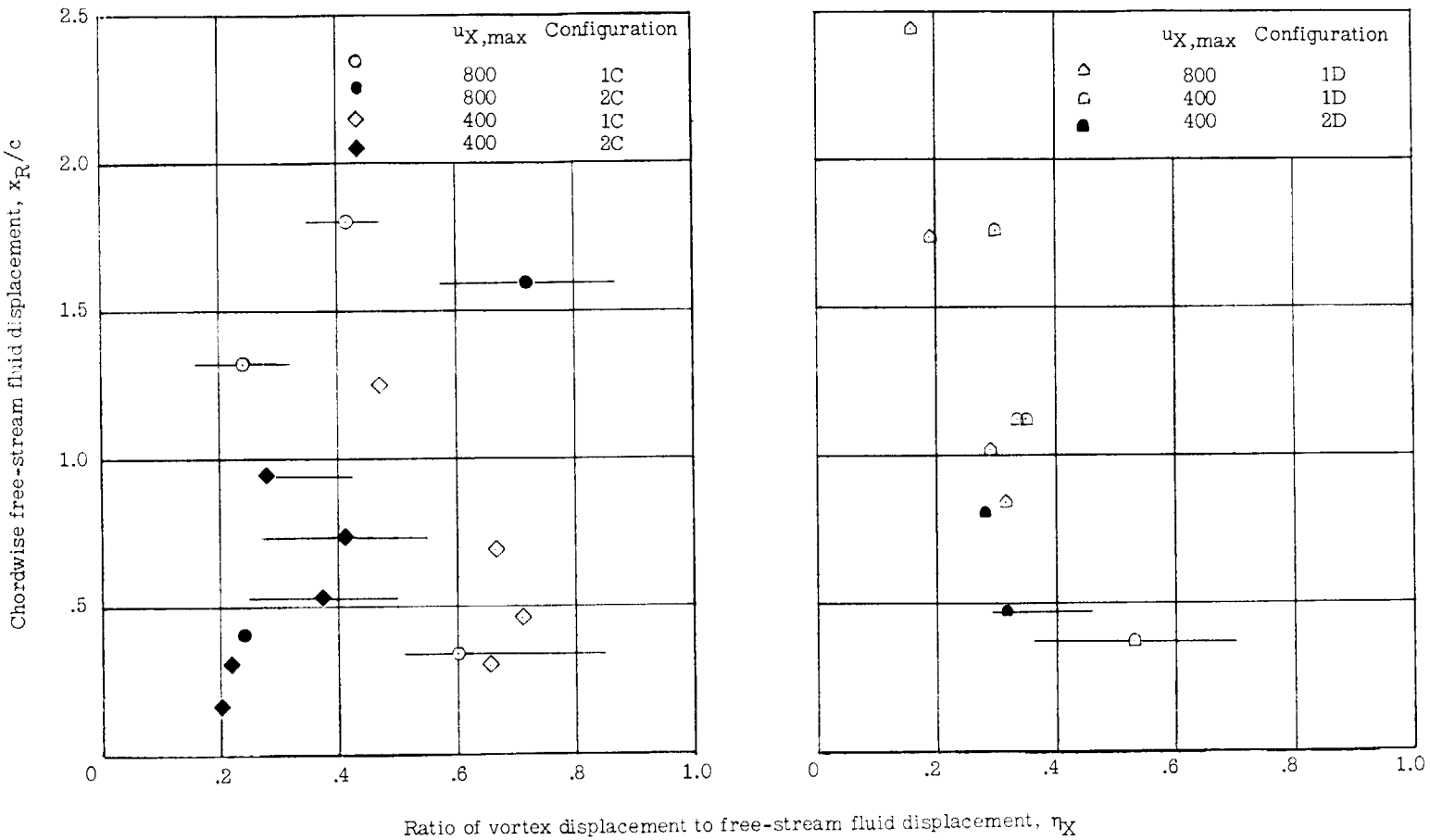

(a) Chordwise components; blast with flow. (b) Chordwise components; blast alone (30°).

Figure 10.- Ratio of leading-edge vortex displacement to free-stream fluid displacement as a function of free-stream displacement for orientation. Conditions C and D.

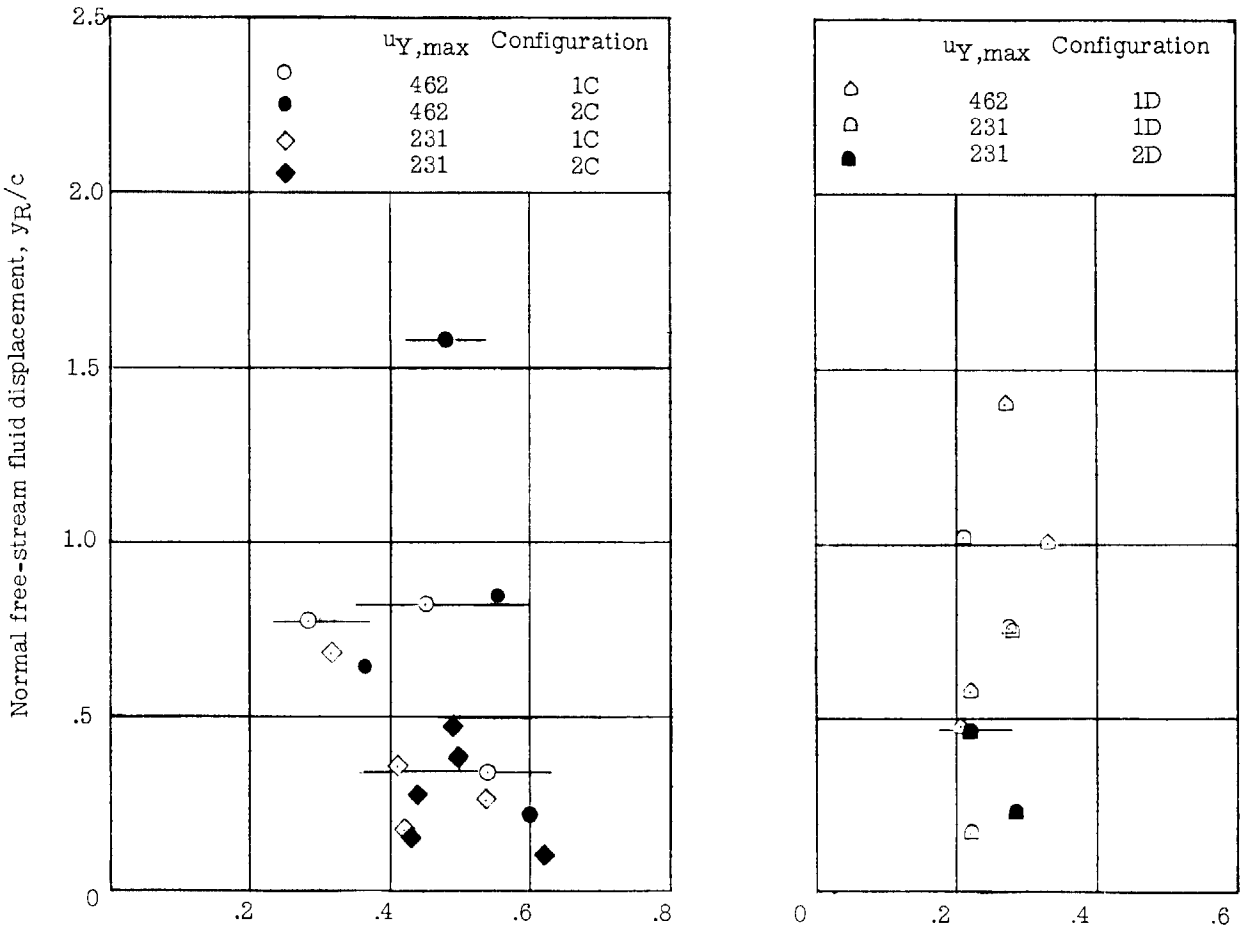

(c) Normal components; blast with flow.

(d) Normal components; blast alone (30°).

Figure 10.- Concluded.

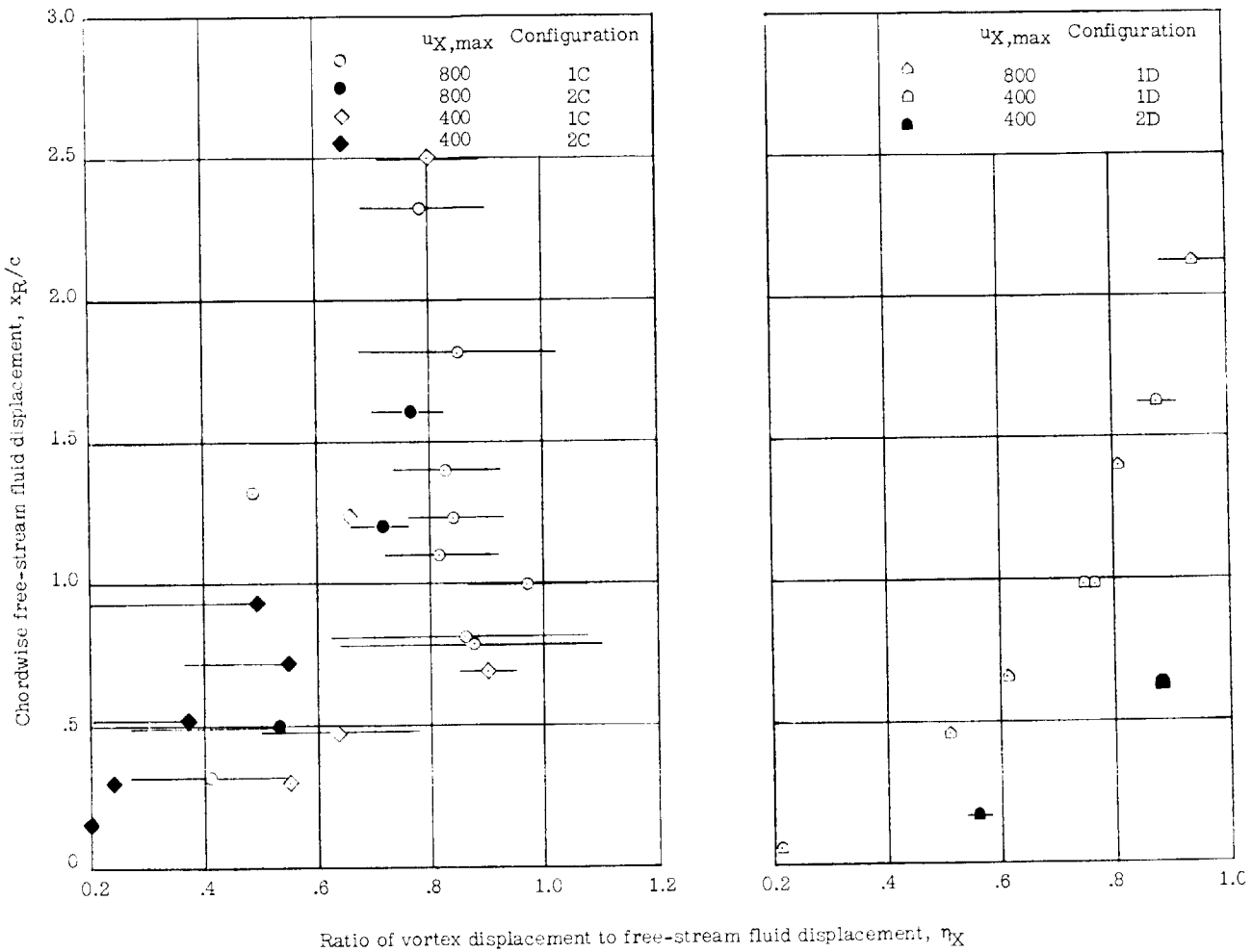

(a) Chordwise components; blast with flow. (b) Chordwise components; blast alone (30°).

Figure 11.- Ratio of trailing-edge vortex displacement to free-stream fluid displacement as a function of free-stream displacement for orientation. Conditions C and D.

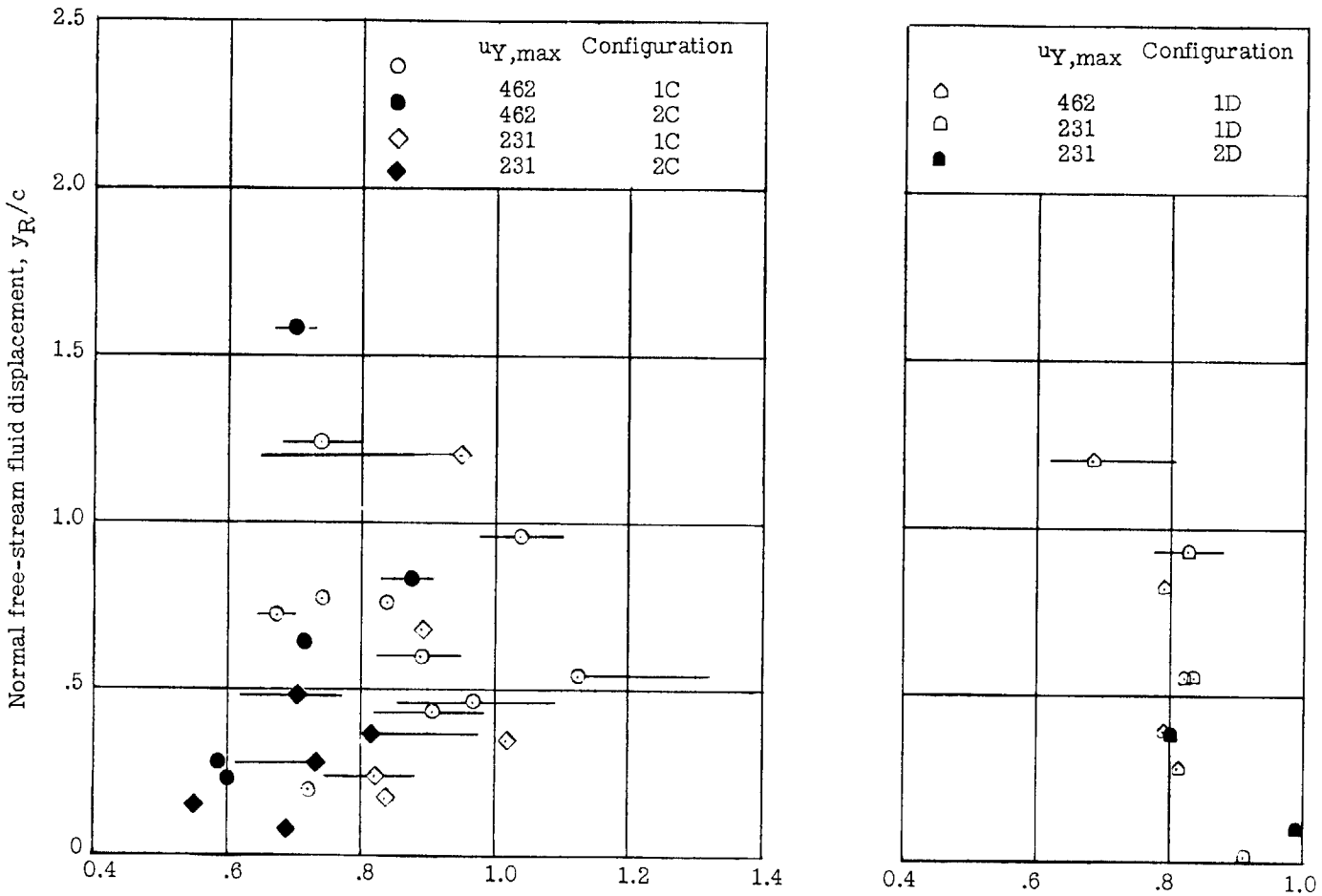

(c) Normal components; blast with flow.

(d) Normal components; blast alone (30°).

Figure 11.- Concluded.

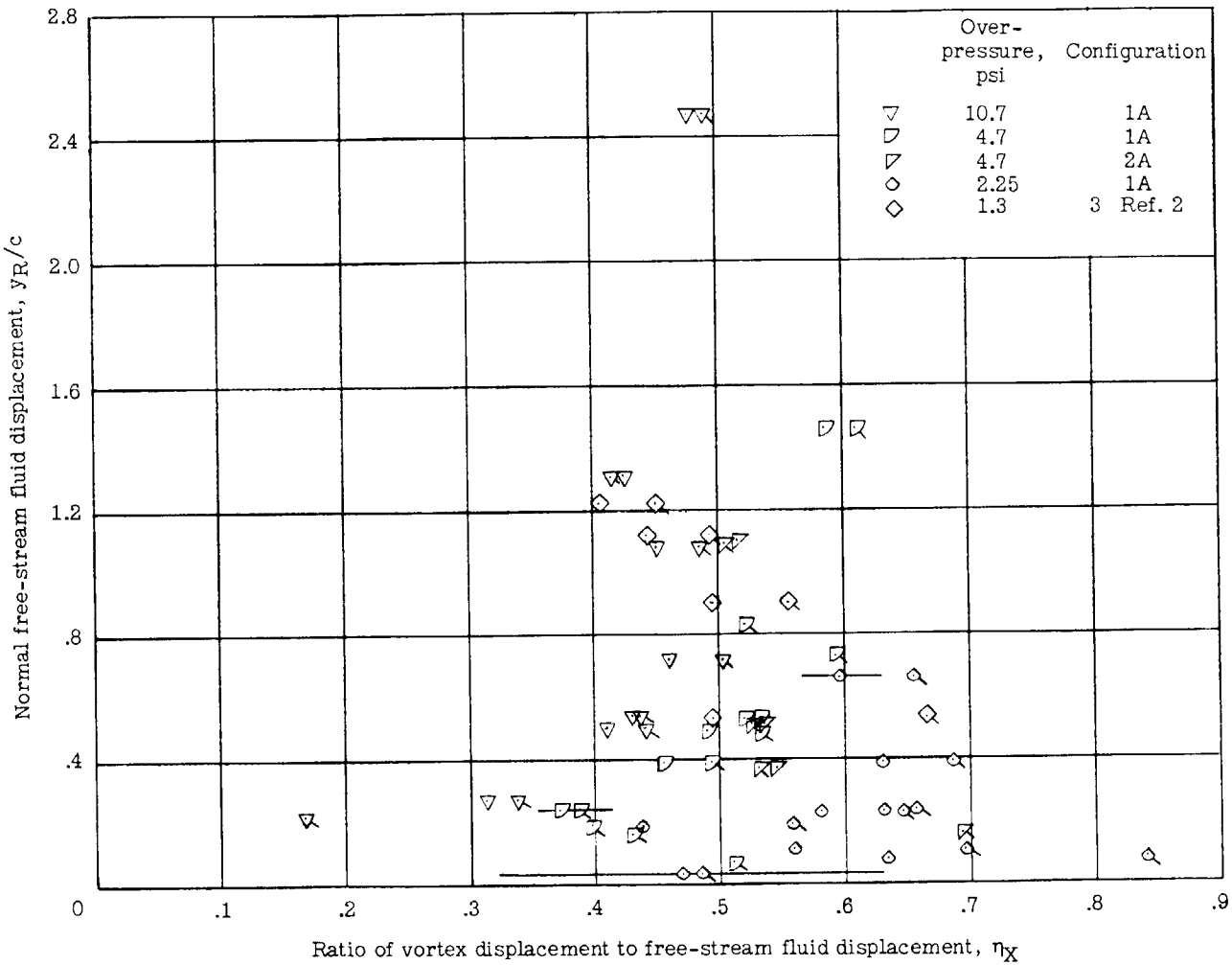

Figure 12.- A comparison of the effect of blast-wave strength on the ratio of vortex displacement to free-stream fluid displacement as a function of free-stream displacement for orientation. Condition A; blast wave alone at 90°. Tails on symbols indicate trailing-edge data.

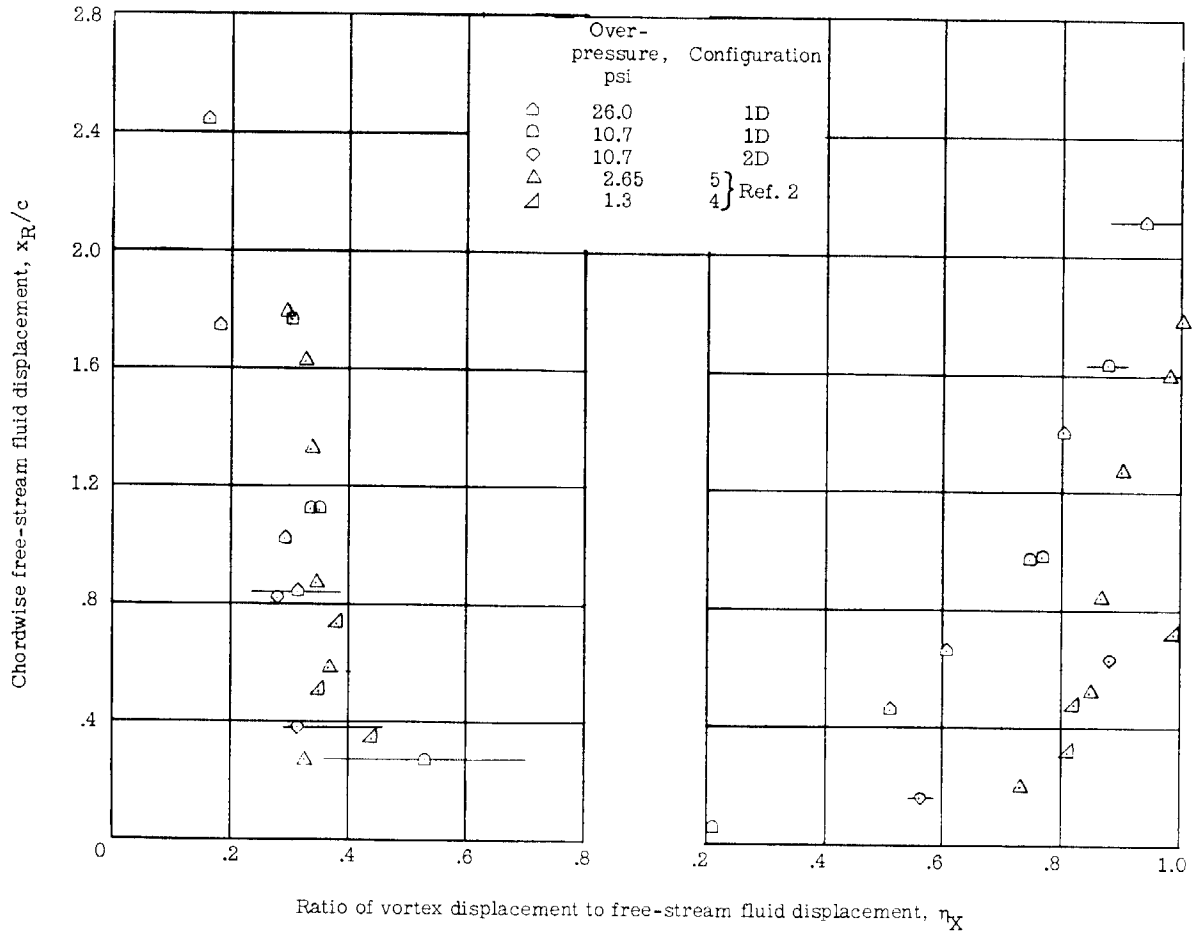

(a) Chordwise components; leading edge. (b) Chordwise components; trailing edge.

Figure 13.- A comparison of the effect of blast-wave strength on the ratio of vortex displacement to free-stream fluid displacement as a function of free-stream displacement for orientation. Condition D; blast wave alone at 30°.

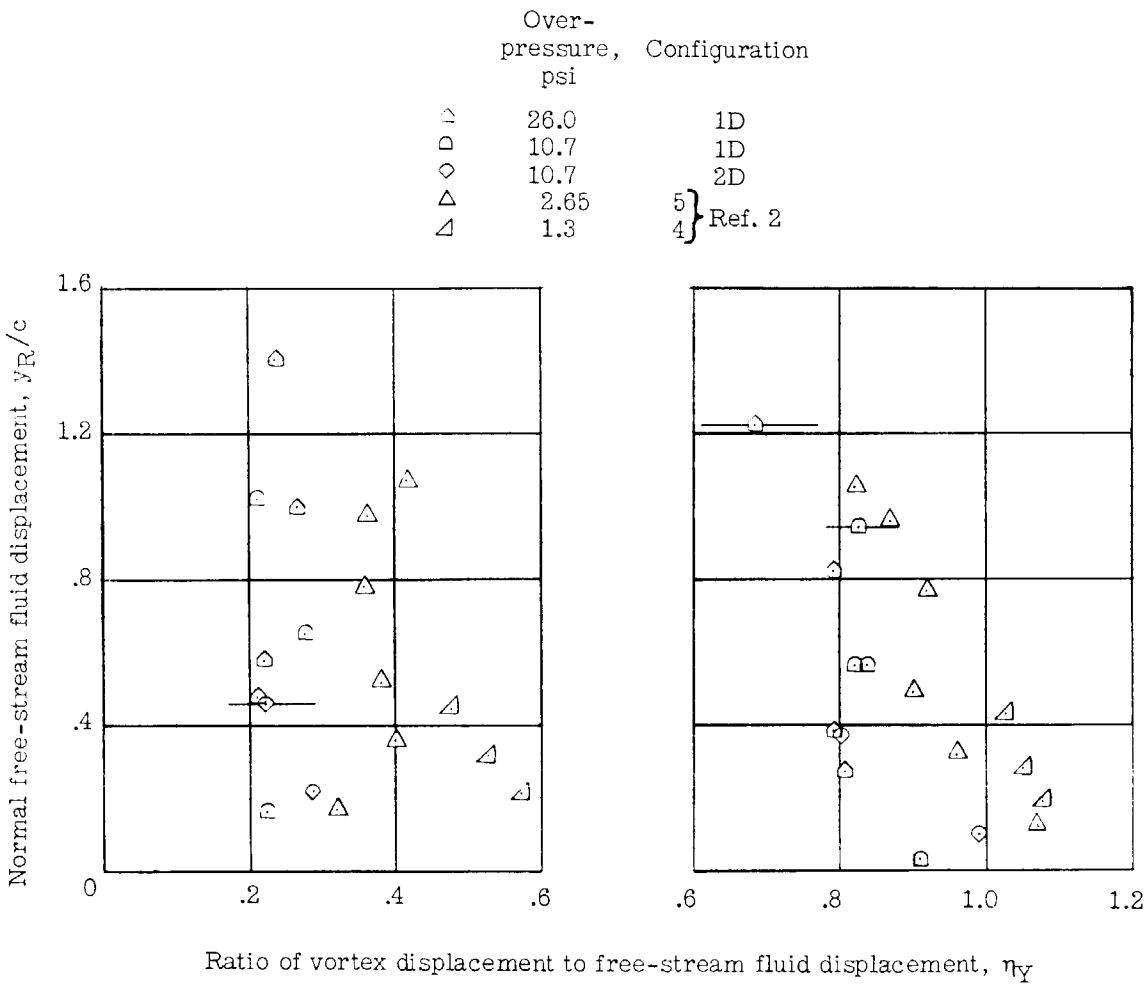

(c) Normal components; leading edge.

(d) Normal components; trailing edge.

Figure 13.- Concluded.

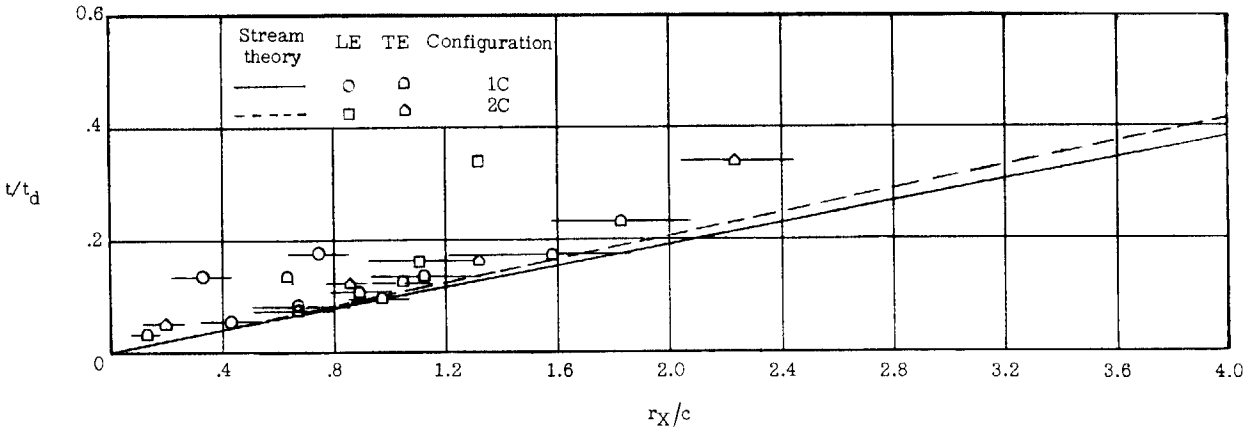

(a) Chordwise components.

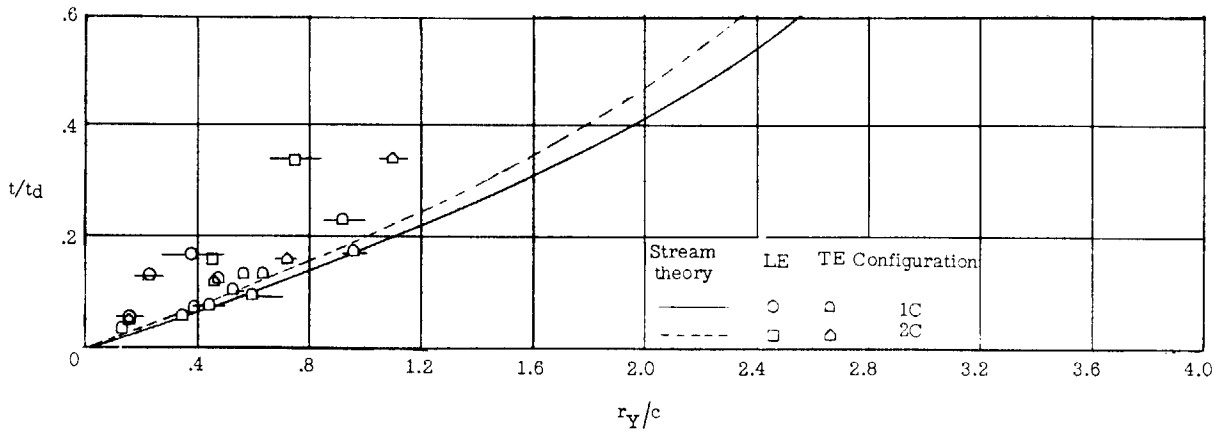

(b) Normal components.

Figure 14.- Vortex position as a function of time for configurations 1 and 2. Orientation condition C1. LE and TE stand for leading edge and trailing edge, respectively.

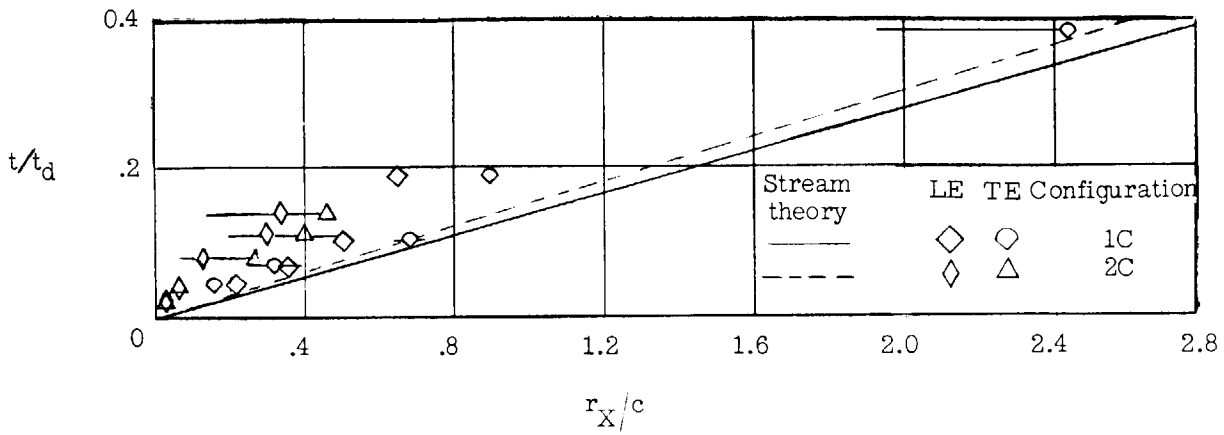

(a) Chordwise components.

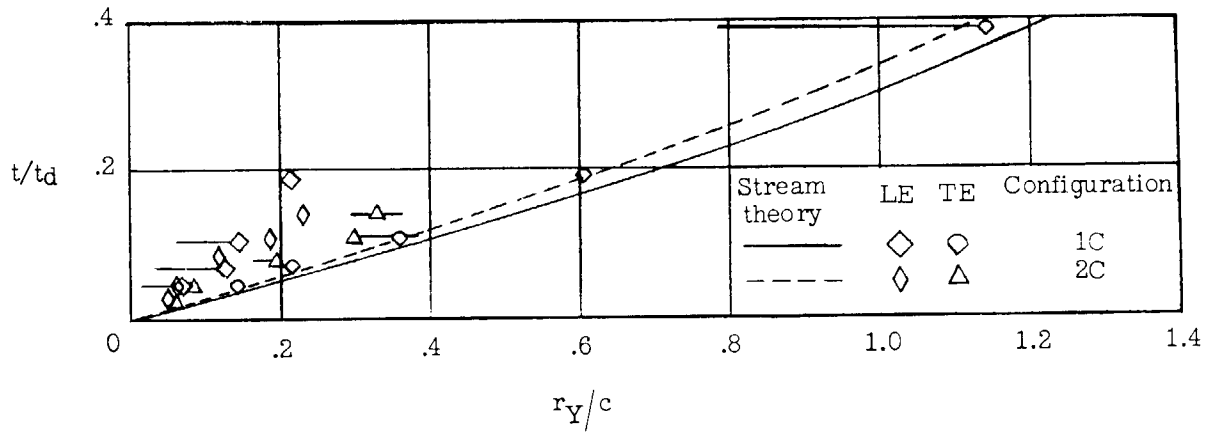

(b) Normal components.

Figure 15.- Vortex position as a function of time for configurations 1 and 2. Orientation condition C2. LE and TE stand for leading edge and trailing edge, respectively.

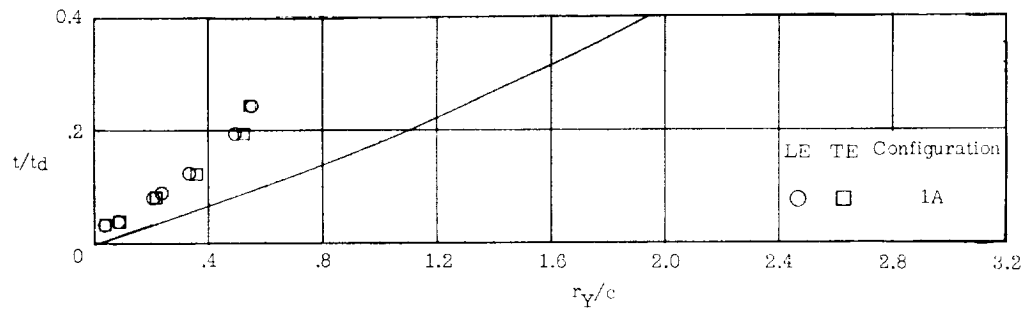

(a) 10.7 pounds per square inch blast wave; condition A1.

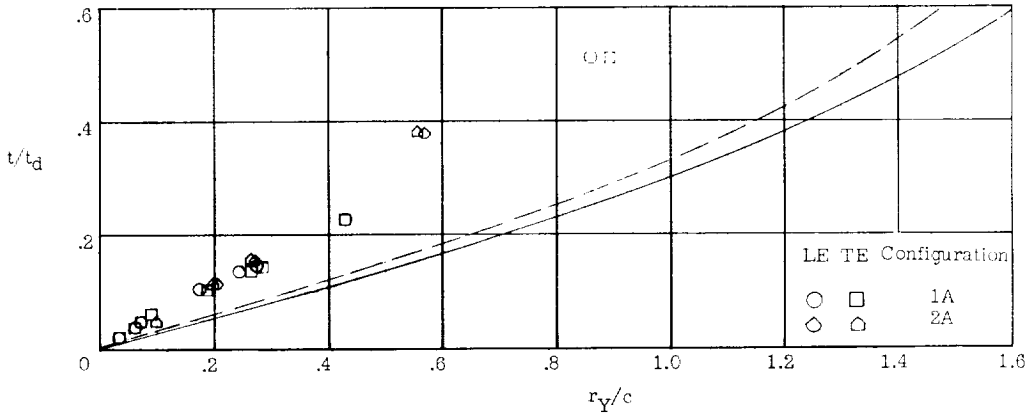

(b) 4.7 pounds per square inch blast wave; condition A2.

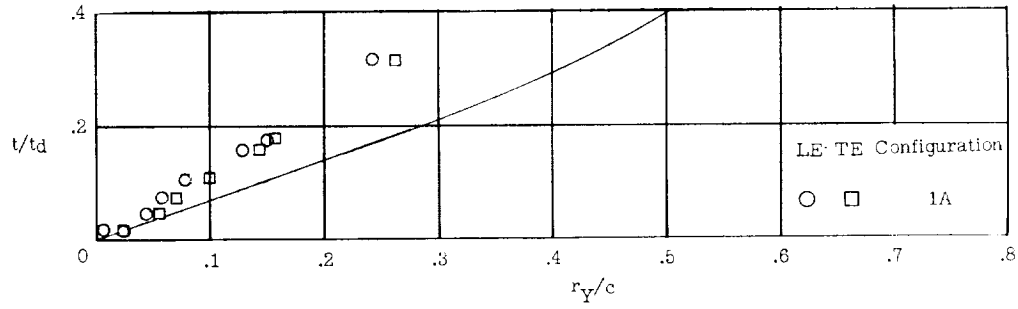

(c) 2.25 pounds per square inch blast wave; condition A3.

Figure 16.- Vortex position as a function of time for a blast wave alone at 90°. LE and TE stand for leading edge and trailing edge, respectively.

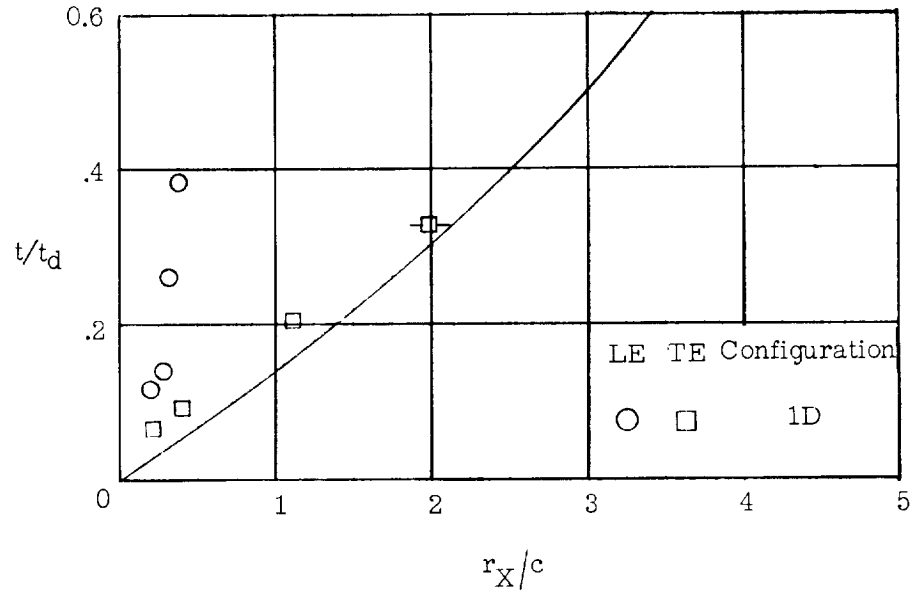

(a) Chordwise components.

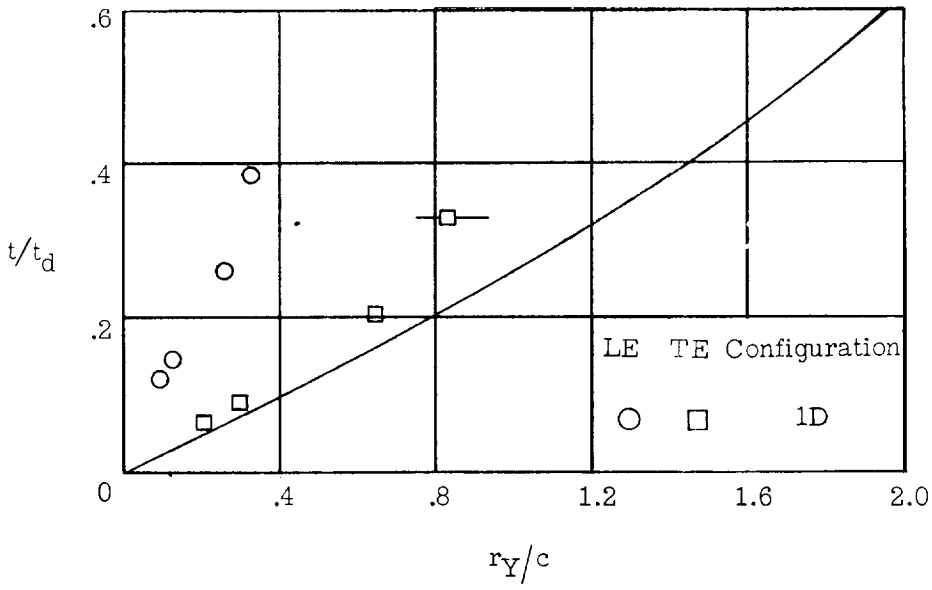

(b) Normal components.

Figure 17.- Vortex position as a function of time for 26 pounds per square inch blast wave at an angle of attack of 30°. Condition D1. LE and TE stand for leading edge and trailing edge, respectively.

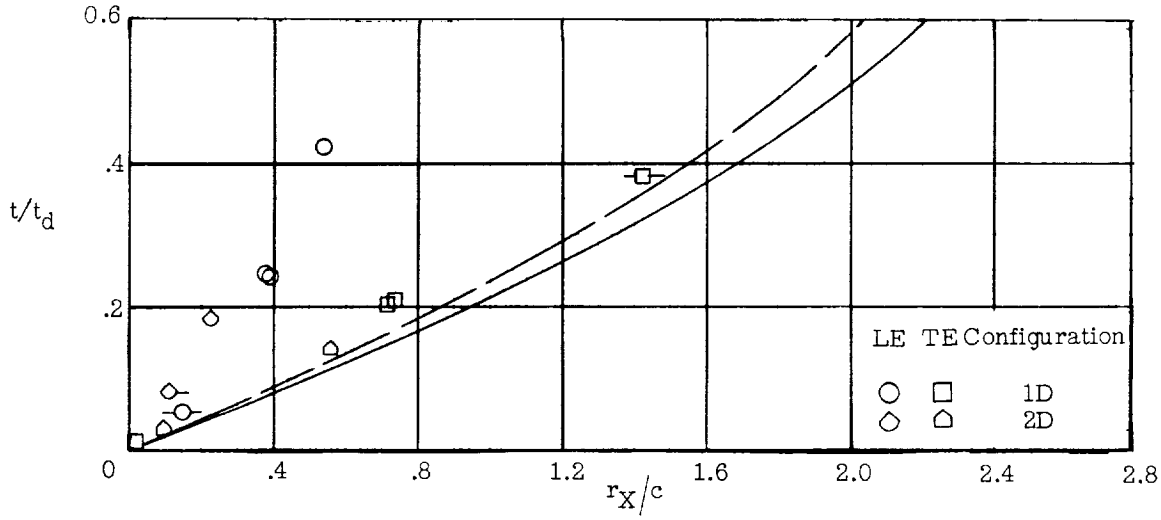

(a) Chordwise components.

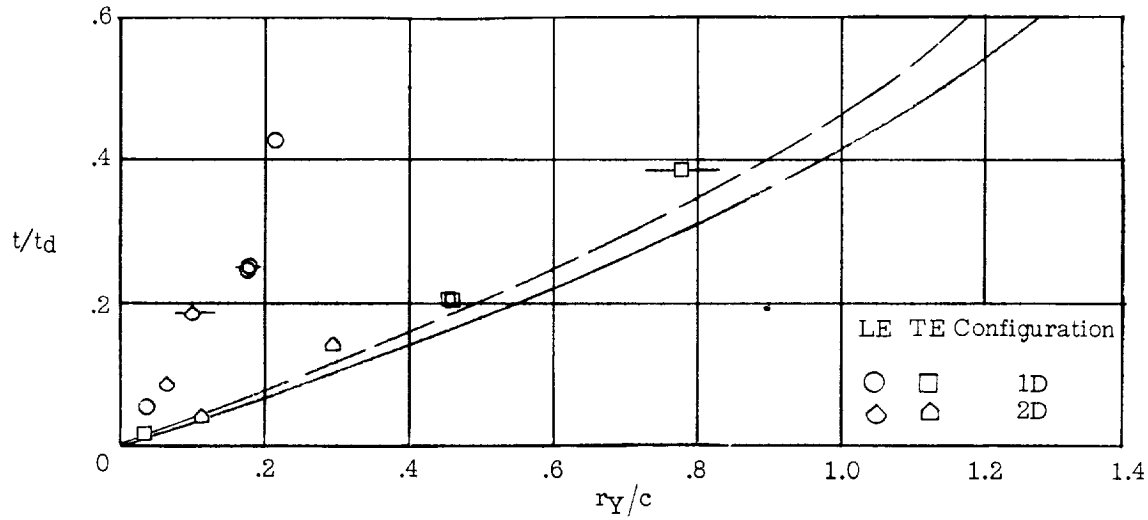

(b) Normal components.

Figure 18.- Vortex position as a function of time for 10.7 pounds per square inch blast wave at an angle of attack of 30°. Condition D2. LE and TE stand for leading edge and trailing edge, respectively.

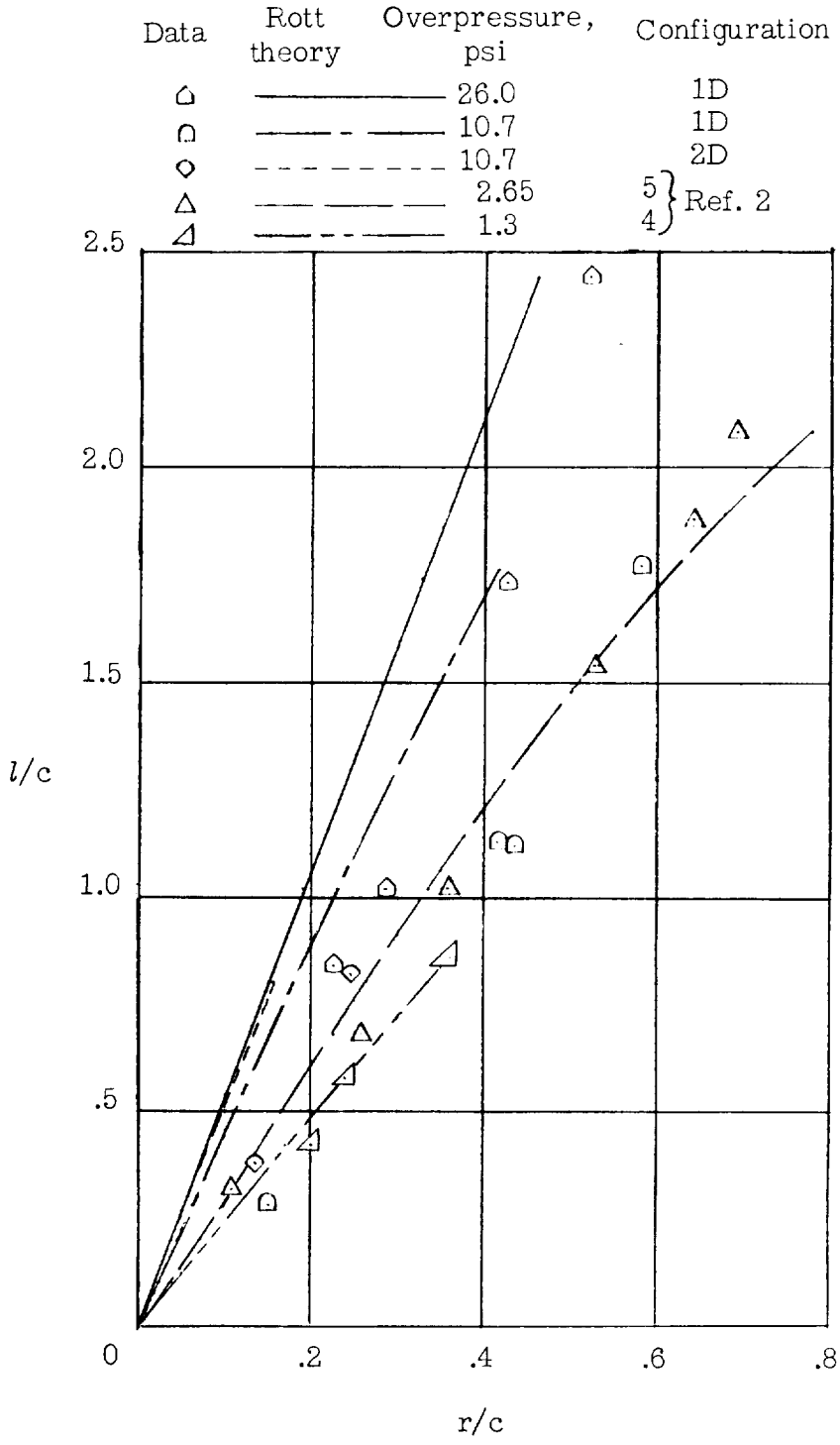

Figure 19.- Comparison of vortex displacement with a modified Rott theory.

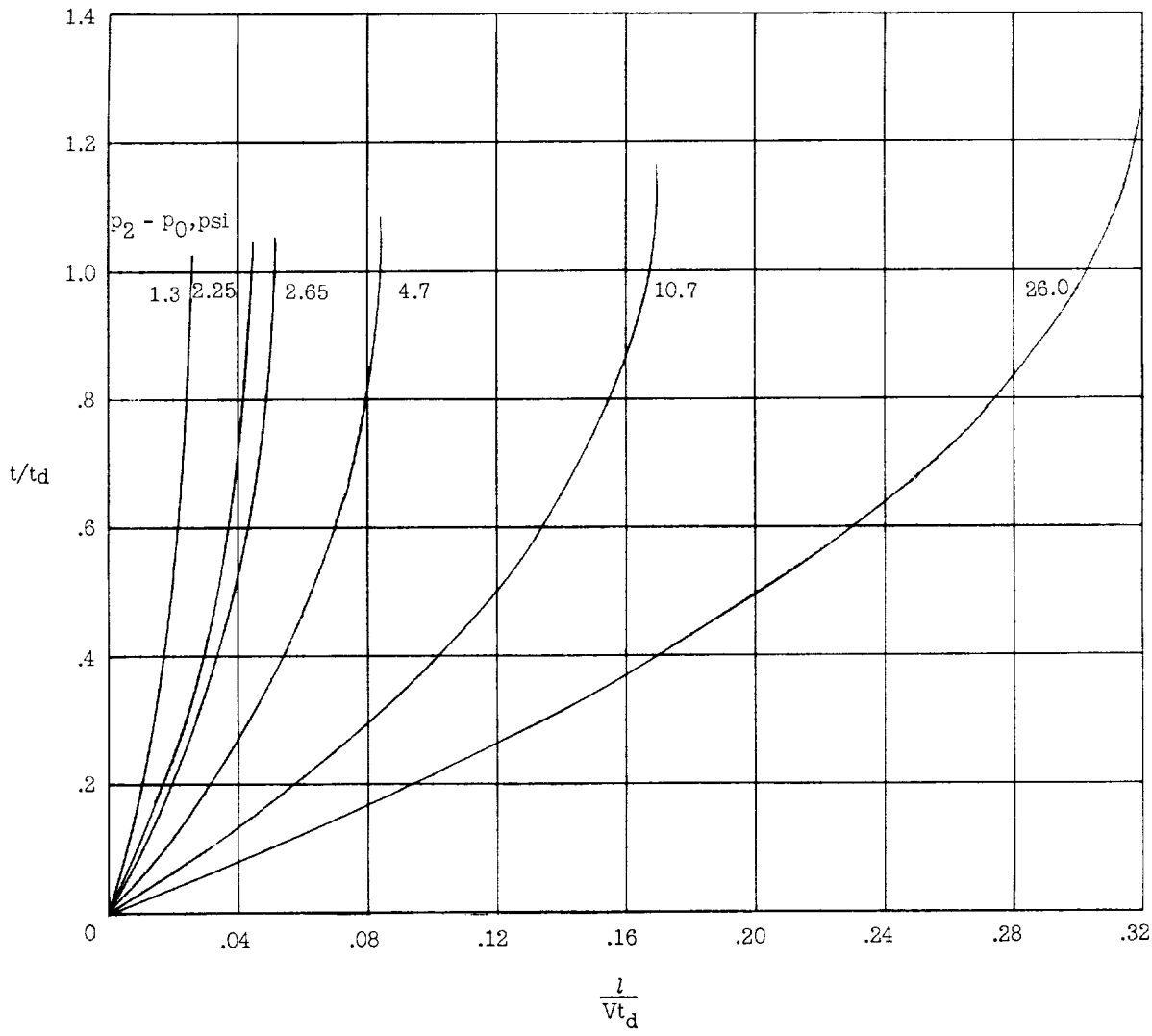

Figure 20.- Nondimensional variation of blast-flow distance with time.

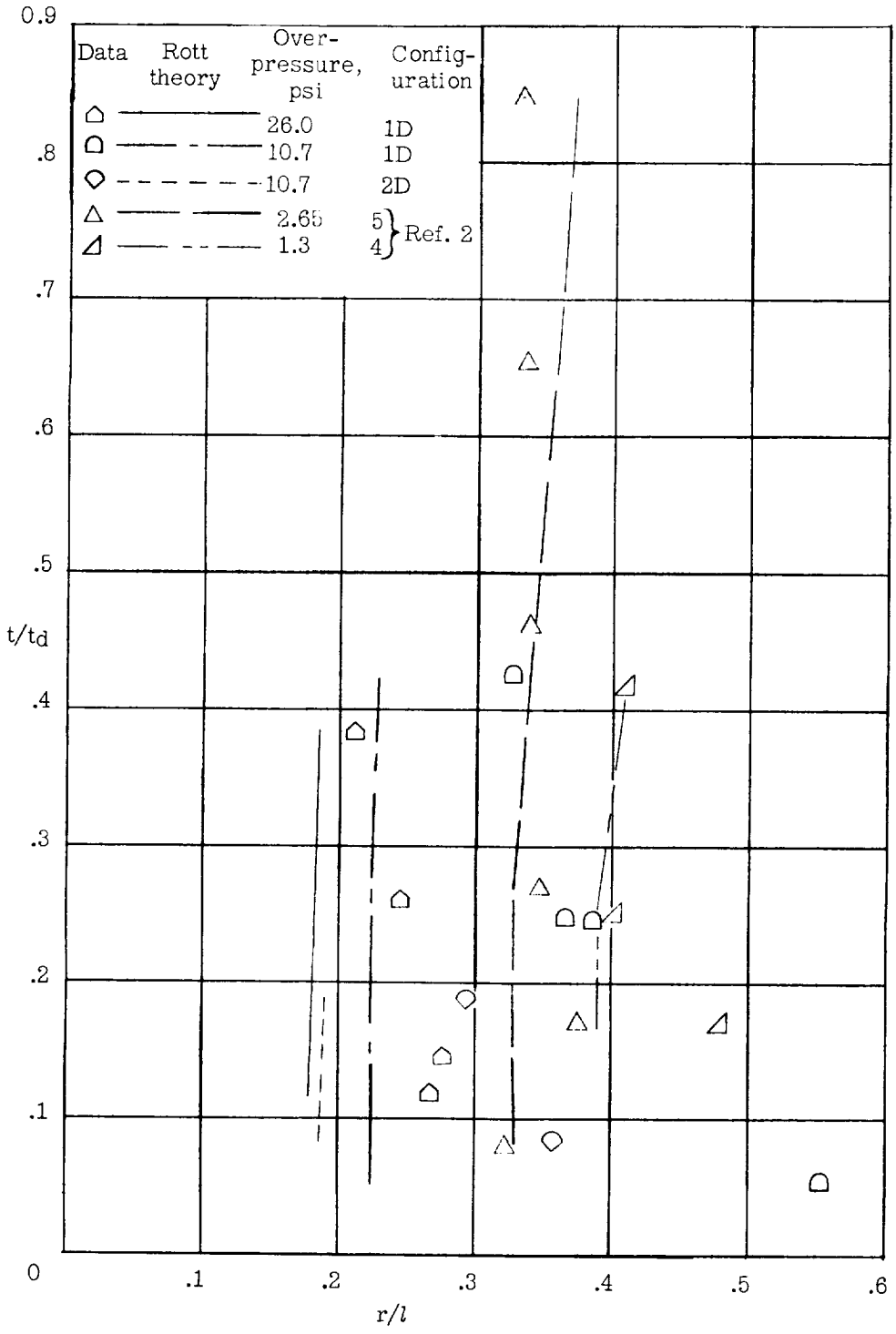

Figure 21.- Comparison of vortex displacement in time with a modified Rott theory.

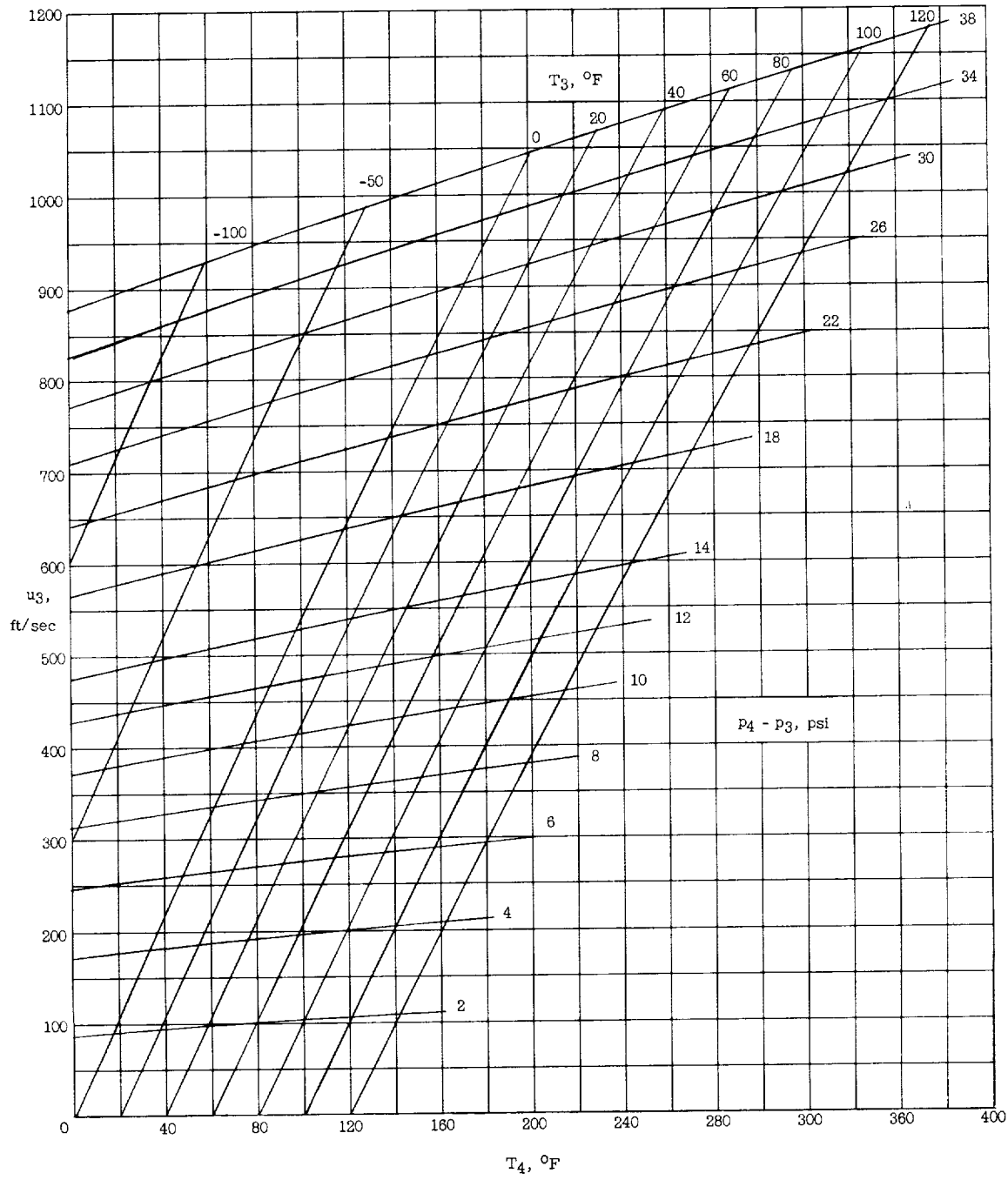

Figure 22.- Plot of shock-driven free-jet relations.

L-686